An Artificial Magnetic Ground-plane for a Log-Periodic Antenna

by

Hugo Hendrik Visser

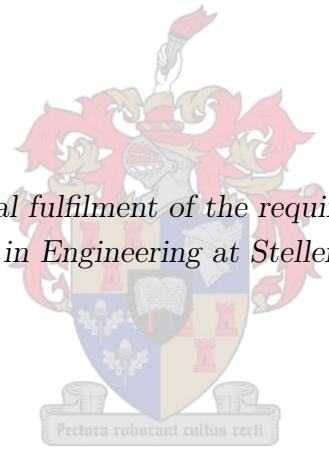

Thesis presented in partial fulfilment of the requirements for the degree of Master of Science in Engineering at Stellenbosch University

Supervisors:

Dr. Riana Helena Geschke
Prof. Keith Duncan Palmer
Department of Electrical and Electronic Engineering

March 2010

Declaration

By submitting this thesis electronically, I declare that the entirety of the work contained therein is my own, original work, that I am the owner of the copyright thereof (unless to the extent explicitly otherwise stated) and that I have not previously in its entirety or in part submitted it for obtaining any qualification.

March 2010

Abstract

This paper presents the implementation of an artificial magnetic ground-plane with a low profile Log-periodic Dipole Array (LPDA) antennas. After the properties of three typical Electromagnetic Bandgap (EBG) structures are investigated and their bandwidth properties are studied, a mechanism is presented to improve the band-width over which the EBG surface acts as a perfect magnetic conductor (PMC). A low profile LPDA is modeled above this surface and the results indicate an improved band-width region. Compared with a LPDA in free space the frequency band is shifted higher by the EBG surface and the gain pattern is shifted from a horizontal orientation to a vertical orientation.

Opsomming

Hierdie dokument stel voor die implementering van kunsmatige magnetiese grondvlakke met Logaritmiese Periodiese Dipool Samestelling (LPDS) antennas. Die eienskappe van drie tipiese Elektromagnetiese Bandgaping (EBG) strukture word ondersoek en hul bandwydte eienskappe word bestudeer. 'n Meganisme word voorgestel om die bandwydte te verbeter waar die EBG oppervlakte soos n perfekte magnetiese geleier optree. 'n Lae profiel LPDS word bo hierdie oppervlakte geplaas. Die resultate dui aan 'n verbetering in the bandwydte. In vergelyking met 'n LPDS in vrye ruimte skuif die frekwensie band hoër as gevolg van die EBG oppervlakte en die aanwins patroon skuif van 'n horisontale orientasie na 'n vertikale orientasie.

Acknowledgements

The author would like to thank the following people for their invaluable contributions to this project:

- Jesus Christ
- Study leaders
- Family
- Friends

Contents

Abbreviations

- AMC - Artificial magnetic conductor
- BPF - Bandpass Filter
- BW - Bandwidth
- CPW - Coplanar Waveguide
- DFT - Discrete Fourier Transform
- EBG - Electromagnetic Band-gap
- EM - Electromagnetic
- FEM - Finite Element Method
- FSS - Frequency Selective Surface
- GHz - Gigahertz
- HIS - High impedance surface
- Hz - Hertz
- JC-EBG - Jerusalem-cross electromagnetic band-gap
- LPDA - Log-periodic dipole array
- MoM - Method of Moments
- PEC - Perfect electric conductor
- PMC - Perfect magnetic conductor
- TE - Transverse Electric
- TEM - Transverse Electric Magnetic
- TM - Transverse Magnetic

List of Figures

List of Tables

Chapter 1

Introduction

1.1 Problem Statement

Electromagnetic Bandgap (EBG) structures are mostly used to suppress surface waves and/or to realise Perfect Magnetic Conductors (PMC) to form an artificial magnetic ground-plane. Most designs operate a usable bandwidth of some 20 % for the inhibition of surface waves, but the bandwidth for PMC operation is typically limited to less than 10 % [2] . The task addressed in this work is twofold:

Firstly, to investigate typical EBG properties with the goal of studying their bandwidth limitations.

Secondly, and more importantly, to propose a mechanism whereby the bandwidth of the PMC operation can be increased for implementation with a LPDA.

1.2 Background

The performance of low profile antennas is degraded by their groundplane backings when the antenna is in close proximity to a groundplane. If the conductor is $\lambda/4$ from the antenna it reflects the antenna radiation in phase, giving approximately a 3 dB increase in gain perpendicular to ground. The problem, however, is that if the conductor is closer than $\lambda/4$ from the antenna it cannot provide the 3 dB increase, because the reflected antenna back-radiation interferes destructively with the antenna forward-radiation. Loosely speaking the antenna can be seen as being partially "short circuited". This is illustrated in Figure 1.1.

A second problem arising when antennas are over ground is the generation of surface waves when a dielectric layer is present. The radiation from the antenna causes surface currents on the conductor. These surface waves impinge negatively on the antenna radiation characteristics.

To solve these problems a Perfect Magnetic Conductor (PMC) would be ideal for low profile antennas. If a surface is lossless and reflects without a phase-shift it can be considered a PMC. A PMC is unfortunately theoretical and can't be realised. However a conductor can be designed to act as a PMC over a certain frequency band. These surfaces are called EBG surfaces or Artificial Magnetic Conductors (AMC). The EBG is a high impedance surface (HIS) and nearly lossless within a certain bandgap and thus acts as a magnetic conductor. The incident wave is

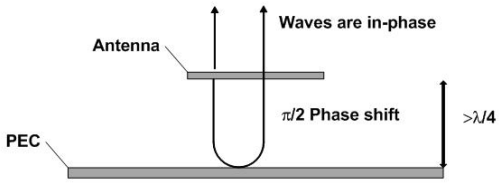

(a) Antenna over PEC with in-phase reflection

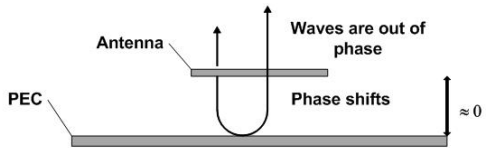

(b) Antenna over PEC with out of phase reflection

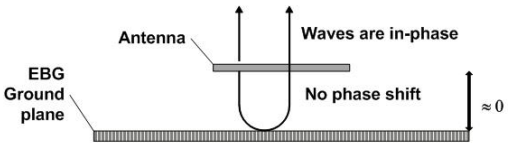

(c) Antenna over EBG

Figure 1.1: Effect of a PEC and EBG backing on an antenna

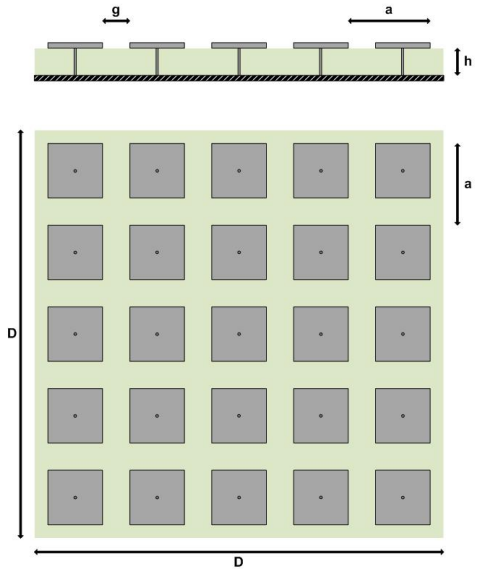

Figure 1.2: Top and side view of the Mushroom EBG

reflected with no phase-shift and the surface waves are suppressed in the structure because of the high impedance. This makes it possible to put the new EBG conductor close to the antenna without the destructive phase limitation.

There are two bandgap regions which need to be considered [2]. The first one is caused as a result of the EBGs array resonance and array periodicity. This is the region where surface waves are suppressed. The second region is caused by the cavity resonance between the ground plane and the HIS. The result is that waves are reflected with no phase shift.

The most commonly known EBG surface is the mushroom EBG [1], Figure 1.2. It consists of a array of metal patches, each patch connected with a via to ground through a substrate. The capacitively-coupled metal patches and inductive vias create a grid of LC resonators. Vias

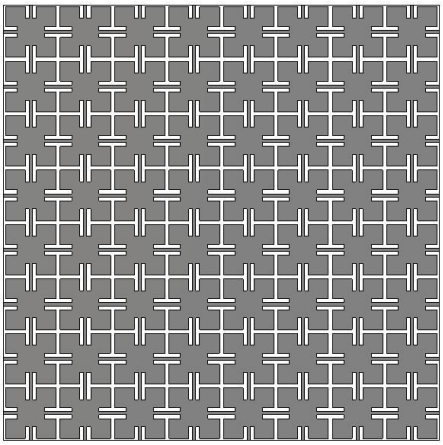

Figure 1.3: Top view of the JC-EBG

in this structure makes fabrication more difficult and costly than a purely planar topology.

To simplify fabrication, a planar EBG can be designed which does not have vias and acts as a periodic frequency selective surface (FSS). A widely used EBG surface, such as this, is the Jerusalem-cross [4], figure 1.3. The JC-EBG consists of metal pads connected with narrow lines to create a LC network.

A key problem with EBGs is that it is difficult to create a broad bandgap and thus it is difficult to combine them with broadband antennas. The following steps are taken to realise a wide-band combination:

- Three EBG surfaces are considered for implementation with a low profile antenna in Chapter 3. These three surfaces are the mushroom EBG, the JC-EBG and the dumbbell EBG. The performances of these EBGs are evaluated.
- The mushroom EBG is selected and modeled in combination with a low profile dipole antenna. Placing a dipole close to a perfect electric conductor (PEC) degrades its performance. With the mushroom surface as groundplane the dipole's performance is restored.
- To study the wide-band performance a scaled mushroom EBG is modeled along with a LPDA. It is revealed that scaling the mushroom cells along with each dipole element of the LPDA gives a good broadband result.

Chapter 2

Modeling Techniques for EBGs

2.1 Introduction

Using computational packages to run simulations is time consuming. To save a lot of design time a good analytical model is needed. Having a good analytical model helps to simplify the design process and yields quicker results.

This chapter will discuss some theoretical models and interpretations of EBGs. Some of these models will be used later in predicting EBG characteristics in order to simplify the design process. The focus of these models will mainly be on the mushroom EBG [1], since it is simple and widely used.

2.2 LC Model

As long as the metal patches in Figure 1.2 are much smaller than the wavelength, the structure can be modeled using lumped elements. The gap, g, between the patches provides the capacitance, while the patches connected with the vias create a current loop which provides the inductance. This is illustrated in Figure 2.1. The impedance of such a parallel LC circuit is:

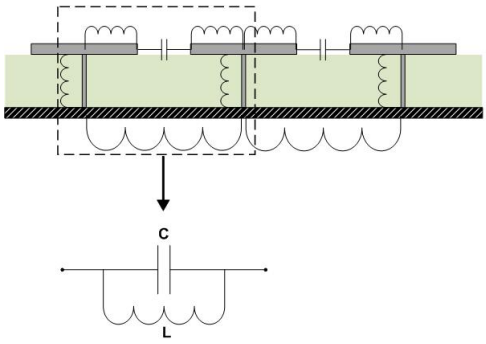

Figure 2.1: Equivalent circuit model for Mushroom EBG

$$Z = \frac{j\omega L}{1 - \omega^2 LC} \tag{2.2.1}$$

where L is the inductance, C the capacitance and ω the radian frequency. The model is inductive at low frequencies (supports TM surface waves) and capacitive at high frequencies (supports TE surface waves). It is at the resonance frequency, f_0, where the impedance is highest.

$$f_0 = \frac{1}{2\pi\sqrt{LC}} \tag{2.2.2}$$

The model is expected to act as a PMC at this frequency.

Two metal patches with gap, g, width, w, and period, a, is shown in Figure 2.2. It is assumed that $g \ll a$ and that there is a voltage difference of V between the patches. The structure lies on top of a substrate, ϵ_r, and is surrounded by air on top, $\epsilon_0 = 1$. The edge capacitance can be derived [1] and is given by:

$$C = \frac{w(\epsilon_0 + \epsilon_r)}{\pi} \cosh^{-1}\left(\frac{a}{g}\right) \tag{2.2.3}$$

The sheet capacitance and inductance, derived in [1], for the whole structure is given as,

$$C_{sheet} = \epsilon h \tag{2.2.4}$$

$$L_{sheet} = \mu h \tag{2.2.5}$$

where μ is the permeability. The reflection coefficient is,

$$R = \frac{Z - 1}{Z + 1} \tag{2.2.6}$$

While this model is accurate for the prediction of the centre frequency of the stopband, it is not accurate in predicting the high impedance bandgap. Some uniplaner EBGs have more complex dimensions for each patch, like the JC-EBG. In [7] more detail is available for calculating LC values for more complex uni-planar EBG geometries.

Expanding this model also does not give more insight into the behaviour of EBGs. Using transmission line theory [11] an expanded model is shown, Figure 2.3.

Each part of Figure 2.3 represents a part of the mushroom EBG. The gap capacitance, C_g, can be calculated using (2.2.3). The line section represents the microstrip before connecting to the via. The equations to calculate C_l and L_l are [11]:

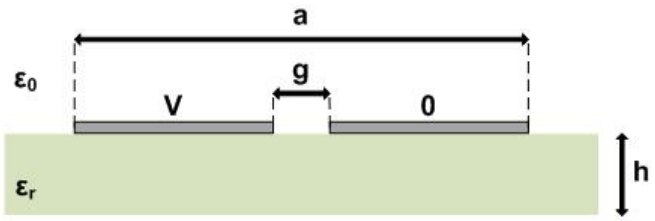

Figure 2.2: Geometry of edge coupled metal patches [1].

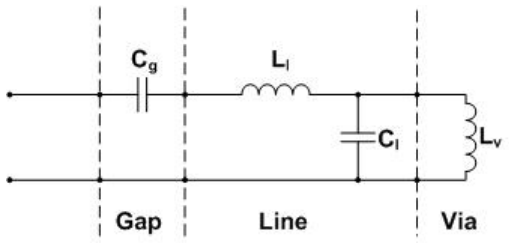

Figure 2.3: Expanded Model of Mushroom EBG

$$\epsilon = \epsilon_r \epsilon_0 \tag{2.2.7}$$

$$\epsilon_e = \frac{\epsilon_r + 1}{2} + \frac{\epsilon_r - 1}{2} \times \frac{1}{\sqrt{1 + 12\frac{h}{w}}} \tag{2.2.8}$$

$$Z_0 = \frac{120\pi}{\sqrt{\epsilon_e}\left[\frac{w}{h} + 1.393 + 0.667 \times \ln\left(\frac{w}{h} + 1.444\right)\right]} \tag{2.2.9}$$

$$Z_0 = \sqrt{\frac{L_l}{C_l}} \tag{2.2.10}$$

$$C_l = \frac{\epsilon A}{h} \tag{2.2.11}$$

With ϵ_e the effective permittivity, Z_0 the characteristic impedance, h the height above ground and w the width of the patch (in our case $a - g$). By calculating Z_0 and C_l, L_l can be obtained by (2.2.10). To calculate the inductance through the via, the following equation is used [9]:

$$L_v = 2 \times 10^{-7} h \left[ln\left(\frac{4h}{d}\right) + 0.5\left(\frac{d}{h}\right) - 0.75 \right] \tag{2.2.12}$$

with d the diameter of the via. The mushroom EBG is a symmetrical structure, therefore only half of the patch is considered for the model. This however does not give a more accurate representation of the Mushroom behaviour. There are more accurate transmission line models available [9] [10], as well as a JC-EBG model [12], but it won't be discussed further. Instead another model to predict the reflection phase will be discussed in Section 2.3.

2.3 Reflection Phase Analytical Model

The next model presented [13] is a model that predicts the reflection phase of the mushroom EBG accurately. The model uses the grid impedance, Z_g, of dense arrays of square patches on a ground plane. The grid impedance is the relation of the total tangential electric field acting on the grid, $\hat{E}^{tot}$, and the average surface current density, $\hat{J}$, induced by the plane wave.

Consider a grid of parallel thin wires excited by a plane wave, Figure 2.4 [14]. With d the separation distance between wires, r_0 the radius of the wires, Z the impedance per unit length and I the current of the wires. Assume that the wire radius and distance is small compared to the wavelength, $kr_0 \ll 1$ and $r_0 \ll d$ respectively. The wave number components of the incident field are as follows:

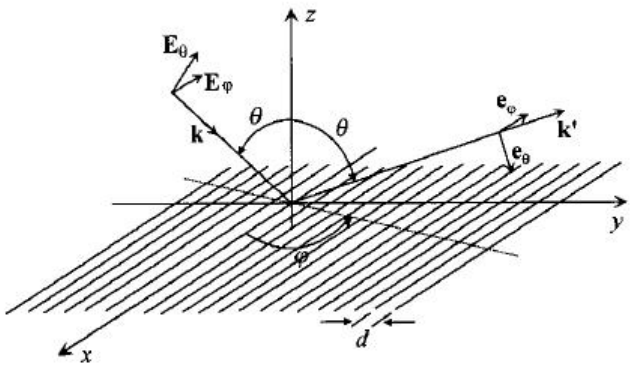

Figure 2.4: The geometry of the planar regular array of wires, taken from [14].

$$\begin{aligned} k_x &= k\, sin\theta\, cos\varphi \\ k_y &= k\, sin\theta\, sin\varphi \\ k_z &= -k\, cos\theta \end{aligned} \tag{2.3.1}$$

where k is the wave number, $k = \omega\sqrt{\epsilon_0\mu_0}$. By using the wire at $y = 0$ as reference the component of the electric field created by the wire is given by [14]:

$$E_{x0}^{w} = -\frac{\eta}{4k}\left(k^2 - k_x^2\right) I e^{-jk_x x} H_0^{(2)}\left(\sqrt{k^2 - k_x^2}\, r_0\right) \tag{2.3.2}$$

where $H_\alpha^{(2)}(x)$ is the Hankel function of the second kind (see Appendix A.1) and η the wave impedance, $\eta = \sqrt{\mu_0/\epsilon_0}$.

Keeping the reference wire at $y = 0$ the local field which acts on the wire currents [14] can be calculated,

$$E_x^{loc} = E_x e^{-jk_x x} - \frac{\eta}{2k}\left(k^2 - k_x^2\right) I e^{-jk_x x} \sum_{n=1}^{\infty} cos\left(k_y nd\right) H_0^{(2)}\left(\sqrt{k^2 - k_x^2}\, nd\right) \tag{2.3.3}$$

The first term gives the incident field and the sum gives the interaction of the fields created by the array. Now that the interaction of the fields are known an expression for the boundary condition can be formulated [14]:

$$E_x^{loc} + E_{x0}^{w} = ZI^{-jk_x x} \tag{2.3.4}$$

This boundary condition implies that when the wire is an ideal conductor ($Z = 0$) there is no tangential electric field on the wire surface and if not ($Z \neq 0$) it is the relationship between the voltage and current along the wire per unit length. By inserting (2.3.2) and (2.3.3) into (2.3.4) the expression is as follows:

$$ZI = E_x - \frac{\eta}{2k}\left(k^2 - k_x^2\right) I\left\{ \frac{1}{|k_Z|\, d} + \frac{j}{\pi}\left[log\frac{d}{2\pi r_0} + \frac{1}{2}\sum_{n=-\infty}^{\infty}{}' \left(\frac{2\pi}{\sqrt{\left(2\pi n + k_y d\right)^2 - \left(k^2 - k_x^2\right) d^2}} - \frac{1}{|n|} \right) \right] \right\} \tag{2.3.5}$$

See Appendix A.2 for the full derivation of (2.3.5). Working towards Z_g the average surface current density is still needed. By introducing the average surface current density, $\hat{J} = I/d$, and inserting (2.3.5) the average current density can be formulated as [14]:

$$\hat{J} = \frac{2}{\eta} \frac{\frac{|k_z|}{k}}{\left(1 - \frac{k_x^2}{k^2}\right)\left(1 + j\alpha\frac{|k_z|}{k}\right) + \frac{2}{\eta}\frac{|k_z|}{k} Zd} E_x \tag{2.3.6}$$

(See Appendix A.3 for simplification) An important parameter is introduced here, α. This is called the grid parameter,

$$\alpha = \frac{kd}{\pi}\left[log\frac{d}{2\pi r_0} + \frac{1}{2}\sum_{n=-\infty}^{\infty}{}' \left(\frac{2\pi}{\sqrt{\left(2\pi n + k_y d\right)^2 - \left(k^2 - k_x^2\right) d^2}} - \frac{1}{|n|} \right) \right] \tag{2.3.7}$$

For dense grids where $k_y d \ll 2\pi$ and $\sqrt{k^2 - k_x^2} d \ll 2\pi$, there is little correction on the logarithmic term. Hence (2.3.7) can be simplified to:

$$\alpha_{ABC} = \frac{kd}{\pi}\, log\frac{d}{2\pi r_0} \tag{2.3.8}$$

where ABC stands for averaged boundary condition. This grid parameter is for thin wires and should be altered to incorporate patches. Each wire can be replaced by metal strips (Figure 2.5 (a)) with width $w = 4r_0 = g$, thus changing equation 2.3.8 to [14]

$$\alpha_{ABC} = \frac{ka}{\pi}\, log\frac{2a}{\pi g} \tag{2.3.9}$$

For a normal incidence-wave polarised along the metal strips the grid impedance for TM and TE polarised fields are as follow [13]:

$$\begin{aligned} Z_g^{TM} &= j\frac{\eta_{eff}}{2}\alpha\left(1 - \frac{k_0^2}{k_{eff}^2}\frac{sin^2\theta}{2}\right) \\ Z_g^{TE} &= j\frac{\eta_{eff}}{2}\alpha \end{aligned} \tag{2.3.10}$$

To this point only the metal strips have been considered and not the patches, therefore the complimentary grid impedance should be calculated (Figure 2.5 (b)). For this purpose Babinet's principle is used. Babinet's principle is used to find complimentary impedances and is as follow:

$$Z.Z' = \frac{\eta_{eff}^2}{4} \tag{2.3.11}$$

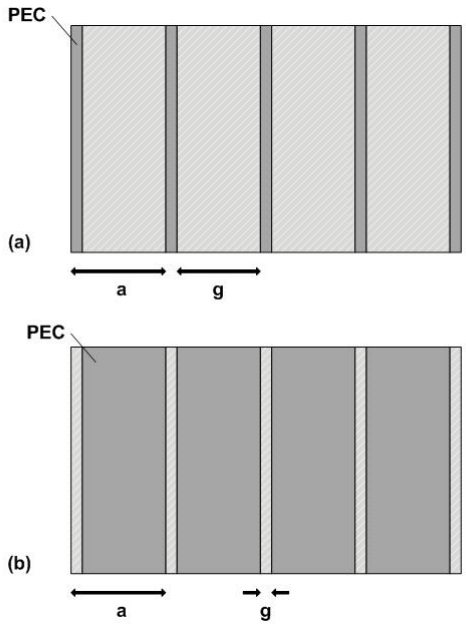

Figure 2.5: (a) Wire grid replaced with metal strips. (b) Complementary grid of (a)

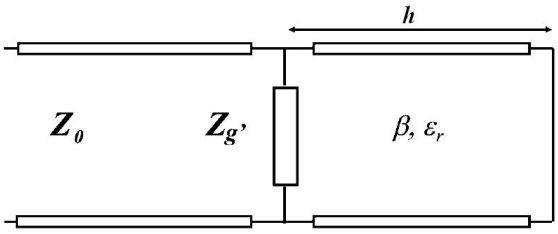

Figure 2.6: The transmission-line model for an array of patches on top of a metal-backed dielectric slab [13].

Z' is the complementary impedance. By applying Babinet's principle to the equations (2.3.10) the complimentary TE and TM polarised grid impedances can be calculated,

$$\begin{aligned} Z_{g'}^{TM} &= -j\frac{\eta_{eff}}{2\alpha} \\ Z_{g'}^{TE} &= -j\frac{\eta_{eff}}{2\alpha\left(1-\frac{k_0^2}{k_{eff}^2}\frac{sin^2\theta}{2}\right)} \end{aligned} \tag{2.3.12}$$

The transmission-line model used to predict the reflection phase is shown in Figure 2.6. This is a model for an array of patches to represent the mushroom EBG. Z_0 is the free space impedance, $Z_{g'}$ is the grid impedance of the array of patches (Equation 2.3.12), h is the height above ground, β is the propagation constant and ϵ_r the relative permittivity.

The input impedance is the parallel combination of the grid impedance and the surface

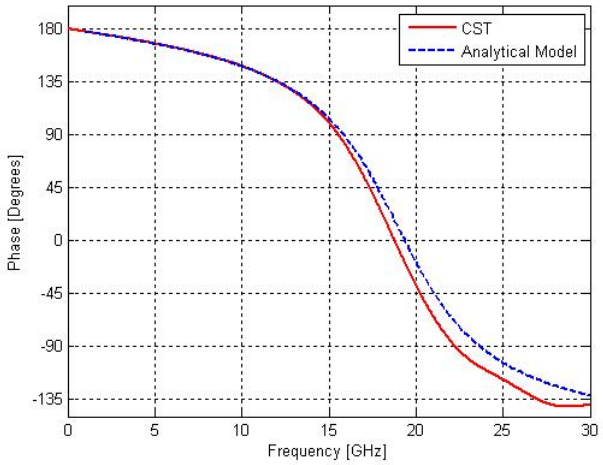

Figure 2.7: Reflection phase of the mushroom EBG

impedance of the grounded dielectric layer,

$$Z_{inp}^{-1} = Z_{g'}^{-1} + Z_s^{-1} \tag{2.3.13}$$

The surface impedance is [14]:

$$Z_s^{TE} = j\omega\mu\frac{tan\beta h}{\beta} \tag{2.3.14}$$

For the TE case substituting (2.3.12) and (2.3.14) into (2.3.13) results in:

$$Z_{inp}^{TE} = \frac{j\omega\mu\frac{tan(\beta h)}{\beta}}{1 - 2k_{eff}\,\alpha\,\frac{tan(\beta h)}{\beta}\left(1 - \frac{1}{\epsilon_r+1}sin^2\theta\right)} \tag{2.3.15}$$

See Appendix A4 for the full derivation. For normal incidence ($\theta = 0$) and no losses, the following equations apply:

$$\mu = \mu_0$$
$$\beta = \omega\sqrt{\mu\,\epsilon_0\,\epsilon_r}$$
$$\epsilon_{eff} = \frac{\epsilon_r + 1}{2}$$
$$k_{eff} = \omega\sqrt{\mu\,\epsilon_0\,\epsilon_{eff}}$$
$$Z_0 = \eta_0$$

Finally, to calculate the reflection:

$$R = \frac{Z_{inp}^{TE} - Z_0}{Z_{inp}^{TE} + Z_0} \tag{2.3.16}$$

Consider a mushroom structure with the following dimensions: a = 3.5 mm, g = 0.5 mm, h = 1 mm and $\epsilon_r = 2.2$. Figure 2.7 shows the reflection phase of this analytical model versus a model designed in CST Microwave Studio. The results compare well with only a 1 % error.

2.4 Conclusion

This chapter illustrated that there are some analytical models available that predict EBG behaviour. While the model of Section 2.2 predicts the centre frequency, it is inadequate in predicting the high impedance bandgap. The model of Section 2.3 predicts the reflection phase of a mushroom EBG accurately.

It is good to have these models from which a design can be launched. Having a general idea of how the EBG will perform makes the design process easier and saves time for not having to run computational simulations over and over. There are however aspects which cannot be predicted by these models and need to be simulated. The next chapter will focus on some simulations of various EBG surfaces.

Chapter 3

Properties of Three Typical EBG Topologies

3.1 Introduction

This chapter investigates the properties of three different EBG structures: the mushroom, JC-EBG and the dumbbell. These three structures were considered as potential candidates below an antenna. The design procedure and simulation results of all three structures will be discussed. The three aspects considered for each EBG surface is the design, the dispersion relation and the reflection phase. Lastly a parameter sweep is done of the reflection phase to illustrate how certain variables influence the EBG performance. The focus will be on the mushroom EBG for it is used in later chapters for implementation. The simulation setup is discussed in Appendix B.

3.2 The Jerusalem-cross EBG

3.2.1 Design

The Jerusalem Cross EBG is a uni-planar structure. It was first presented in [17]. It consists of metal patches connected on all four sides with a narrow line. Where the patch and the line connect there is an inset to increase the inductance. The narrow lines provide the structure with inductance while the separation between the patches provides the capacitance. Because this is a uni-planar structure there are no vias connected to ground. The LC nature creates a high impedance region where surface waves are suppressed. Figure 3.1(a) shows a single cell JC-EBG, while figure 3.1(b) shows an array of 8x8 JC-EBG cells which is used for the s-parameter simulation.

For the simulation in CST Microwave Studio the following dimensions are used:

- $a = 3.5\,mm$ (Period of unit cell)
- $g = 0.5\,mm$ (Gap width)
- $w = 0.2\,mm$ (Width of inductor line)

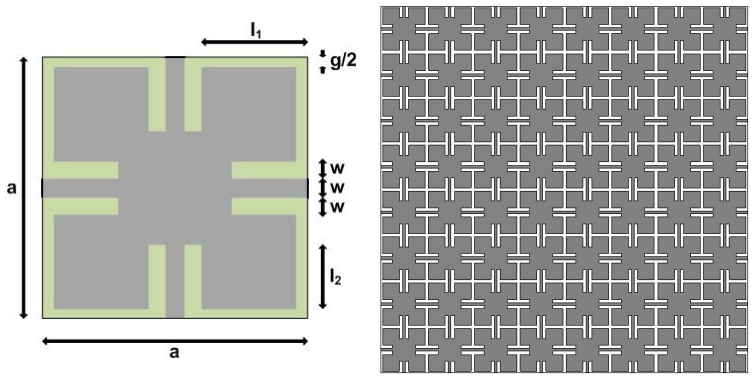

(a) Top view of a single cell JC-EBG (b) Top view of a JC-EBG array

Figure 3.1: The jerusalem cross EBG

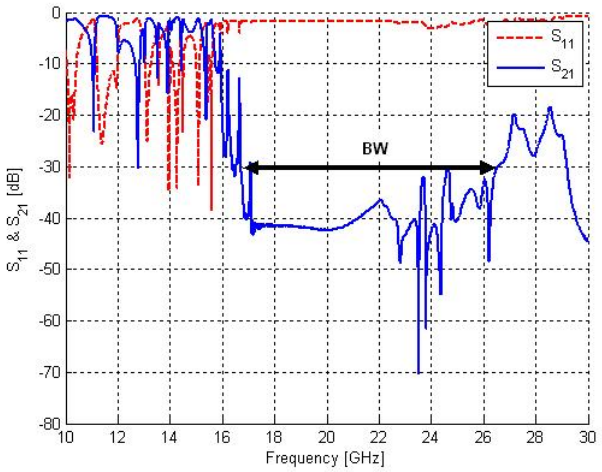

Figure 3.2: Simulated S-parameters of a JC-EBG

- $h = 1\,mm$ (Height above ground)
- $l_1 = \frac{a}{2} - \frac{3 \times w}{2}$ (Length as indicated in figure 3.1(a))
- $l_2 = \frac{a}{4} - \frac{g}{2}$ (Length as indicated in figure 3.1(a))
- $\epsilon_r = 2.2$ (Relative permittivity)

The design parameters are obtained from a parametric study, Chapter 3.5. Calculating the inductance and capacitance amounts to $13.952\,nH$ and $0.107\,pF$ respectively. These figures do not however give a good prediction of the high impedance zone. The s-parameters are simulated and shown in figure 3.2. (See appendix B.1 for the simulation setup).

The bandgap is indicated where the transmission drops below -30 dB. Thus the high impedance region for the JC-EBG starts at 16.72 GHz where the magnitude drops below -30dB and stops at 26.54 GHz.

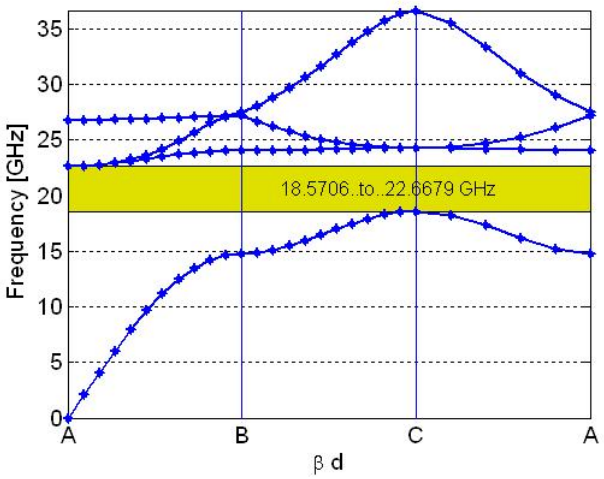

Figure 3.3: TE Dispersion Diagram of a JC-EBG

3.2.2 Dispersion Diagrams

Dispersion diagrams show the dispersion relation of surface waves along the contour of the Brillouin zone and give a good indication of the bandgap of HIS surfaces. Using eigenvalue equations the allowed frequencies for a specific wave vector can be calculated. As stated in [1] a numerical analysis of the dispersion relation of surface waves indicates no bandgap region. Consider therefore a simulation using the eigenmode solver of CST Microwave Studio (see Appendix B.2). The same dimensions as in Section 3.2.1 are used for the model, except that only a single unit cell is needed. The bandgap is the region where no wavenumber exists for the corresponding frequency. Figure 3.3 shows the TE dispersion diagram with a bandgap between 18.6 GHz and 22.7 GHz.

3.2.3 Reflection Phase

Using a technique called time gating the reflection phase was simulated using CST Microwave Studio (see Appendix B.3 for the model setup). This gives a good indication of the band where an incident wave is reflected with no phase reversal. The bandwidth is taken from ±45 degrees [6]. The reflection phase can be seen in figure 3.4. The centre frequency of the simulated model is 23.09 GHz with a bandgap of 6.3 %.

3.3 The Dumbell EBG

3.3.1 Design

The following structure is also a uni-planar EBG and is called the Dumbbell. The dumbbell was first presented in [7]. The thin microstrip bridges provide the inductance, while the small gaps provide the capacitance. As with the JC-EBG the dumbbell has no vias and the LC nature of the structure forms a high impedance region where surface waves are suppressed. Figure 3.5(a)

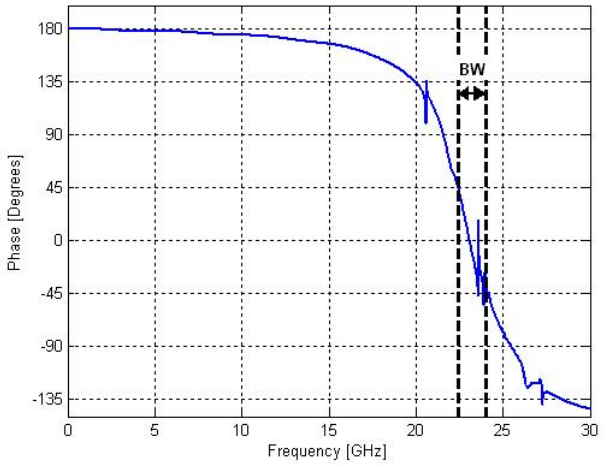

Figure 3.4: Simulated reflection phase and bandwidth of the JC-EBG

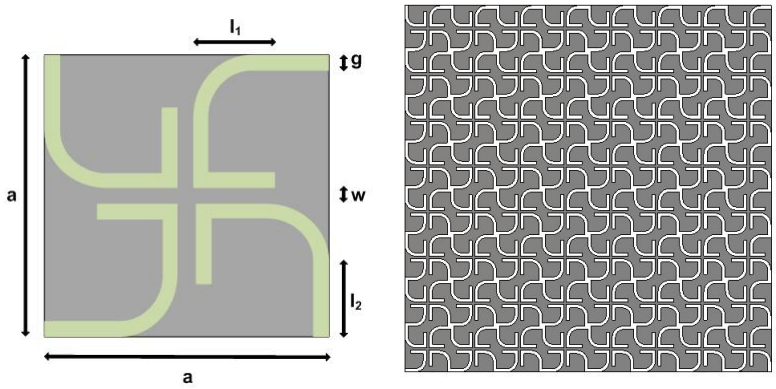

(a) Top view of a single cell dumbbell EBG

(b) Top view of a dumbbell EBG array

Figure 3.5: The dumbbell EBG

shows a single dumbbell cell, while figure 3.5(b) shows an array of 8x8 dumbbell cells which is used for the s-parameter simulation.

For the simulation in CST Microwave Studio the following dimensions are used:

- $a = 3.5\,mm$ (Period of unit cell)
- $g = 0.25\,mm$ (Gap width)
- $w = 0.2\,mm$ (Width of inductor line)
- $h = 1\,mm$ (Height above ground)
- $l_1 = 0.27 \times a$ (Length as indicated in figure 3.5(a))
- $l_2 = \frac{l_1}{1.2}$ (Length as indicated in figure 3.5(a))
- $r = \frac{a}{2} - l_2 - g - \frac{w}{2}$ (Radius of dumbbell arc)

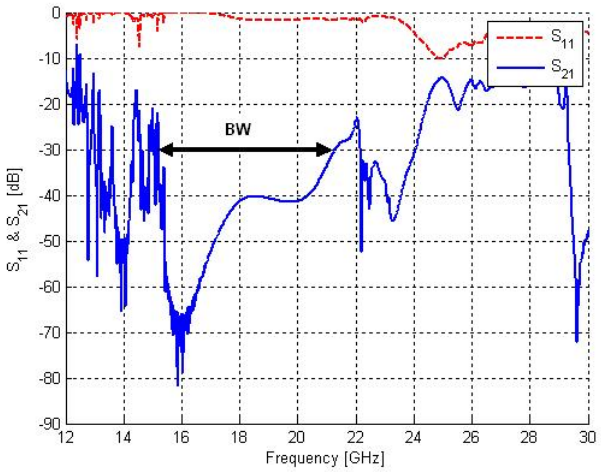

Figure 3.6: Simulated S-parameters of a dumbbell EBG

- $\epsilon_r = 2.2$ (Relative permittivity)

The $\frac{l_1}{l_2}$ ratio should not exceed 1.2 [5]. The design parameters are obtained from a parametric study, Chapter 3.5. Calculating the inductance and capacitance amounts to $0.59\,nH$ and $0.105\,pF$ respectively. Like the JC-EBG these figures do not give a good prediction of the high impedance zone. The s-parameters are simulated and shown in figure 3.6. (See appendix B.1 for the simulation setup).

The bandgap is indicated where the transmission drops below -30 dB. Thus the high impedance region for the dumbbell EBG starts at 15.198 GHz where the magnitude drops below -30dB and stops at 21.29 GHz.

3.3.2 Dispersion Diagrams

Using the same dimensions as in Chapter 3.3.1, except that only a unit cell is needed, a dispersion diagram is plotted using CST Microwave Studio (see Appendix B.2). Figure 3.7 shows the TE dispersion diagram. The bandgap region stretches from 15.4 GHz to 20.7 GHz, which corresponds well with the s_{11} of figure 3.6.

3.3.3 Reflection Phase

A technique called time gating is used again to simulate the reflection phase in CST Microwave Studio (see Appendix B.3 for the model setup). Taking the bandwidth again from ± 45 degrees, the centre frequency of the simulated model is 18.75 GHz with a bandgap of 5.7 %. The reflection phase can be seen in figure 3.8.

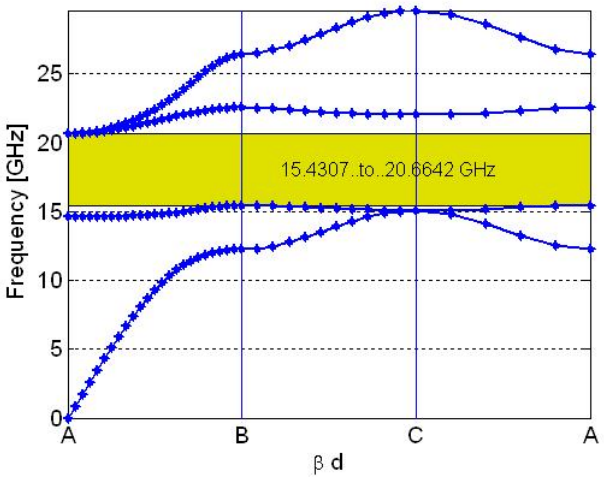

Figure 3.7: TE Dispersion Diagram of a dumbbell EBG

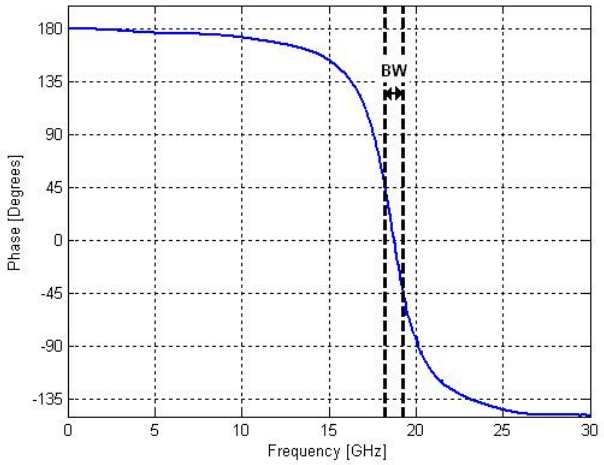

Figure 3.8: Simulated reflection phase and bandwidth of the dumbbell EBG

3.4 The Mushroom EBG

3.4.1 Design

The mushroom EBG was first introduced in [1]. It consists of an array of patches each with a via connecting to a ground plane, figure 1.2. The gaps between the patches give the structure capacitance and the inductance is obtained from the path through the patch, via and ground. This LC combination gives the EBG its PMC nature over a certain bandgap.

Consider a mushroom EBG with the following dimensions: $D = 28\,mm$, $a = 3.5\,mm$, $g = 0.5\,mm$, $h = 1\,mm$, $d = 0.125\,mm$ and $\epsilon_r = 2.2$. The design parameters are obtained from a parametric study, Chapter 3.5. Using equation (2.2.3) and (2.2.5) the capacitance and inductance can be calculated respectively. This amounts to a capacitance of $C = 71.26\,fF$ and an inductance of $H = 1.26\,nH$. Now using equation (2.2.2) the centre frequency is $f_0 = 16.82\,GHz$.

Equation (2.2.1) can now be used to predict where the structure has a high impedance and

is shown in figure 3.9. It can be seen that there is a higher impedance between 12 and 23 GHz, with a significant rise between 16 and 18 GHz and a peak at 16.8 GHz.

Consider a simulation using CST Microwave Studio, figure 3.10. Two discrete ports are used to obtain the s-parameters. A high suppression region can be noticed between 12 GHz and 25.75 GHz where the transmission drops below -30 dB. This compares very well to the predicted high impedance region of figure 3.9.

Around 16 GHz the structure radiates, this can be attributed to the resonance of the patch array. Using the -30 dB mark to indicate the bandgap region it can be seen that the mushroom EBG has a better bandwidth than the JC-EBG and the dumbbell.

3.4.2 Dispersion Diagrams

Using the same dimensions as in Chapter 3.4.1, except that only a unit cell is needed, a dispersion diagram is plotted using CST Microwave Studio (see appendix B.2). Figure 3.11 shows the TE dispersion diagram. The bandgap region stretches from 14 GHz to 16 GHz.

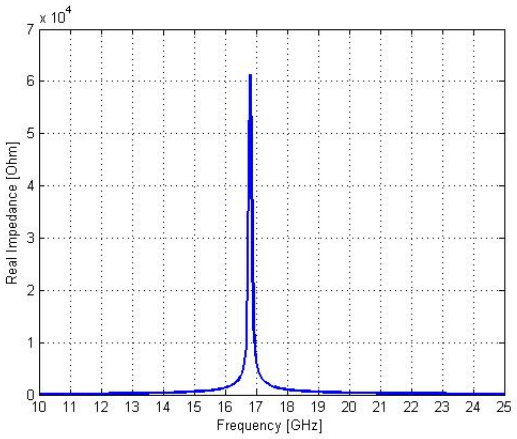

Figure 3.9: Predicted real impedance according to Chapter 2.1.

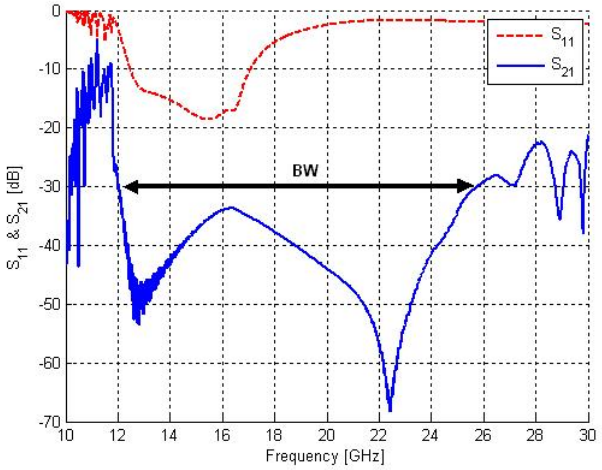

Figure 3.10: Simulated S-parameters of a mushroom EBG

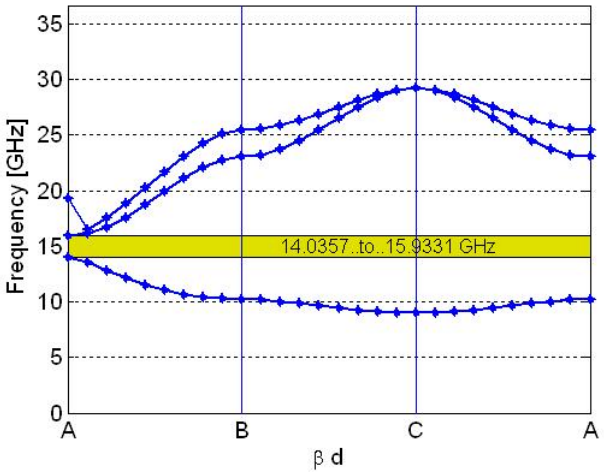

Figure 3.11: TE Dispersion Diagram of a mushroom EBG

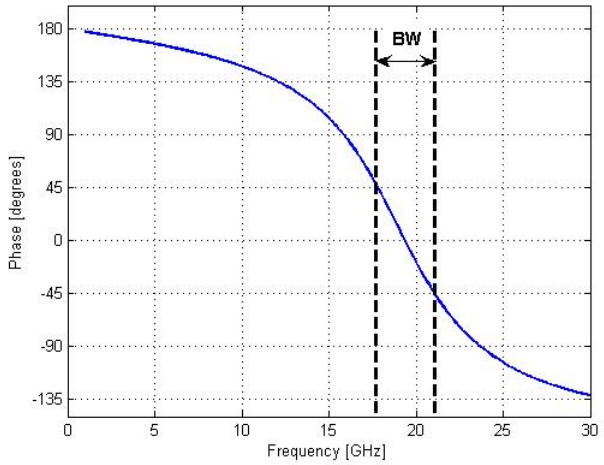

Figure 3.12: Predicted reflection phase and bandwidth

3.4.3 Reflection Phase

Using the model of Chapter 2.3 (equation 2.3.15) the predicted reflection phase can be seen in figure 3.12. Taking the bandgap at ±45 degrees [6], the BW is 17 % at a centre frequency of 19.35 GHz.

Using a technique called time gating the reflection phase was simulated using CST Microwave Studio (see appendix B.3 for the model setup). The reflection phase can be seen in figure 3.13. The centre frequency of the simulated model is 18.76 GHz with a bandgap of 15.5 %.

Comparing the simulated model with the analytical model shows a good correlation between the results. Thus the analytical model is a quick and easy tool to get a accurate indication of the reflection phase of a mushroom EBG model.

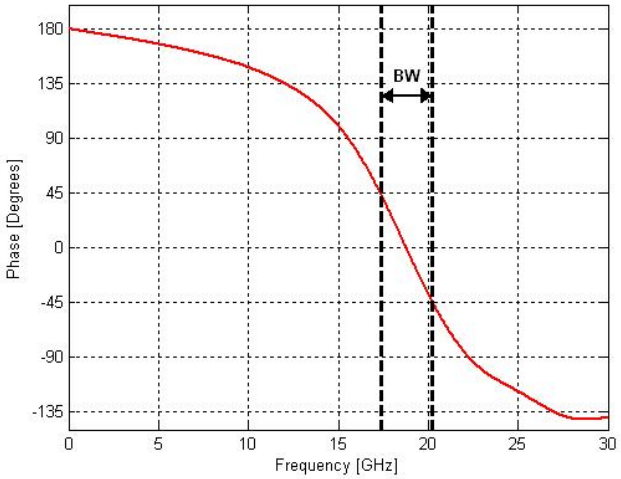

Figure 3.13: Simulated reflection phase and bandwidth of the mushroom EBG

Table 3.1: Parameter sweep of different variables from the JC-EBG

Varying the period							
a $[mm]$	**5**	**6**	**8**	**10**	**12**	**14**	**16.67**
BW $[\%]$	2.4	2.02	1.56	1.29	1.09	0.93	0.83
f_c $[GHz]$	13.62	11.3	8.41	6.63	5.52	4.72	4.11
Varying the gap							
g $[mm]$	**0.05**	**0.1**	**0.2**	**0.4**	**0.5**		
BW $[\%]$	2.14	2.24	2.44	2.15	1.97		
f_c $[GHz]$	12.34	12.46	13.32	14.02	14.25		
Varying the half-inductor length							
$l_2 + \frac{g}{2}$ $[mm]$	**0.5**	**1**	**1.25**	**1.5**	**2**		
BW $[\%]$	3.2	3.34	3.07	2.7	1.74		
f_c $[GHz]$	18.98	16.37	15.32	14.33	12.22		

3.5 Conclusion and Results

A parametric study of the EBG structures gives insight into the influence of certain variables. The study is done on the reflection phase characteristics of the various EBG structures. While one variable is being varied the other remains constant. The results are displayed in Appendix C and a summary of the results is displayed in tables 3.1 to 3.3.

Table 3.1 and figures C.1 and C.2 display the results of the JC-EBG. As the period increases the bandwidth as well as the centre frequency drops. Varying the gap gives a maximum bandwidth at $g = 0.2\,mm$. Increasing the gap also results in a slight increase in the centre frequency. The half-inductor length keeps the bandwidth and centre frequency stable over certain values, but has a significant influence if it is too long or too short. If it is too short the centre frequency rises considerably and if too long it drops. The bandwidth stays consistent but drops significantly when increasing the length.

Table 3.2 and figures C.3 and C.4 display the results of the dumbbell EBG. As the period increases the bandwidth as well as the centre frequency drops. The bandwidth is stable for short periods but then drops significantly when increasing the period. With smaller gaps the

Table 3.2: Parameter sweep of different variables from the dumbbell EBG

Varying the period							
a $[mm]$	**5**	**6**	**8**	**10**	**12**	**14**	**16.67**
BW [%]	1.97	1.93	1.43	0.98	0.79	0.85	0.86
f_c $[GHz]$	14.45	11.85	8.79	7.03	5.81	4.97	4.12
Varying the gap							
g $[mm]$	**0.15**	**0.2**	**0.3**	**0.4**	**0.5**		
BW [%]	3.07	2.38	2.41	2.29	2		
f_c $[GHz]$	11.59	12.33	13.55	14.09	14.34		
Varying the half-inductor length							
l_1 $[mm]$	**0.1**	**0.175**	**0.225**	**0.27**	**0.35**		
BW [%]	2.88	3.03	2.73	2.52	2.21		
f_c $[GHz]$	16.33	15.13	14.27	13.63	12.36		

centre frequency drops and increases the bandwith a bit. The bandwidth is stable when varying the gap. Increasing the half-inductor length decreases the centre frequency and the bandwidth, however the bandwidth shows a maximum at $l = 0.175\,mm$.

Table 3.3 and figures C.5 and C.6 display the results of the mushroom EBG. As expected, increasing the period of a EBG cell decreases the centre frequency, but it also decreases the bandwidth. This trend is the same for all three EBG structures considered. Varying the gap, which contributes to the capacitance, increases the mushroom EBGs bandwith and centre frequency. Varying the height has a big influence on the bandwidth and centre frequency. An increase in height shows an increase in bandwith and a decrease in centre frequency. The via radius has little influence on the bandwidth and centre frequency.

The results make it evident that the main feature for the design is as expected the period. The other variables are then used to fine tune the design. Scaling the variables can give a good indication of where to start the design.

Although the via radius did not have a big influence on the parametric study the via itself still has a big influence on the suppression of TM surface waves [1]. The waves entering the dielectric via-region interact with the vias and as a result slow down the propagation. This suppression helps the reflection phase bandgap to coincide with the bandgap where surface

Table 3.3: Parameter sweep of different variables from the mushroom EBG

Varying the period							
a $[mm]$	**5**	**6**	**8**	**10**	**12**	**14**	**16.67**
BW [%]	5.36	4.67	3.6	2.96	2.54	2.21	1.88
f_c $[GHz]$	12.1	10.51	8.37	6.96	5.95	5.19	4.46
Varying the gap							
g $[mm]$	**0.05**	**0.1**	**0.2**	**0.4**	**0.5**		
BW [%]	4.06	5.05	5.73	6.1	6.3		
f_c **[GHz]**	9.26	11.34	13.25	15	15.6		
Varying the hight							
h $[mm]$	**0.5**	**0.75**	**1**	**1.25**	**1.5**		
BW [%]	5.73	7.54	8.64	9.8	10.85		
f_c **[GHz]**	13.25	11.49	10.16	9.17	8.38		
Varying the via radius							
r $[mm]$	**0.05**	**0.1**	**0.2**	**0.3**	**0.4**		
BW [%]	5.76	5.75	5.73	5.69	5.62		
f_c $[GHz]$	13.13	13.17	13.25	13.39	13.59		

waves are suppressed [2]. Although these bandgaps can coincide with a uni-planar EBG it is not necessarily so.

The goal of this work is to implement an EBG structure below an antenna. Thus the reflection phase characteristics are more important for the design of the EBG because the reflected antenna wave should not have a phase reversal. Suppressing surface waves are also ideal but electromagnetic waves are not restricted just to surface waves that propagate in the horizontal plane and more is needed to determine the bandgap.

When comparing the reflection phase bandwidths of the three EBG structures it is clear that the mushroom EBG is more suitable as a conductor for an antenna than the uni-planar EBGs. The uni-planar EBGs have more suitable applications which include TEM waveguide [18], coplanar waveguide (CPW) [17], compact microstrip bandpass filters (BPFs) [17] and parasitic parallel-plate mode suppression [5] just to name a few.

Chapter 4

Narrow-band Topology: Dipole over a Mushroom EBG

4.1 Introduction

This chapter investigates what happens when placing a low profile dipole above a mushroom EBG. This is a topology popular in the literature [20] [22] [23] and is used to demonstrate the bandwidth limitations when combining an EBG with an antenna in close proximity. The results are compared with the same dipole above a PEC surface. Over a PEC surface the performance of the dipole degrades. The dipole length is also changed above the same mushroom surface to illustrate that a bandgap does exist.

4.2 Design and Results

To test the performance of the mushroom EBG underneath a low profile antenna a small dipole is used. The same mushroom model as Section 3.4 is used. Taking the centre frequency from figure 3.13, $f_c = 18.76\,\text{GHz}$, a dipole is designed. For this frequency the dipole length is calculated as $8\,mm$. Figure 4.1 shows the impedance and return loss of the dipole.

The antenna is placed horizontally $0.5\,mm$ above the mushroom surface at the centre of the array. The positioning of the dipole is not important for it does not influence the results [20]. A simulation is run using FEKO (see Appendix B) and is shown in figure 4.2.

The figure compares four results, namely the dipole itself, the dipole above a mushroom surface, the dipole above a PEC surface and the dipole above a PMC surface. From the results it can be seen that the PEC degrades the dipole performance considerably. It is also evident that the mushroom surface restores the dipole performance well with a small frequency offset and is consistent with the performance above a PMC surface.

To illustrate that the mushroom EBG has a bandwidth where it is operational a $10\,mm$ dipole is used. Again a simulation using FEKO is done. The results are shown in figure 4.3.

The performance of the $10\,mm$ dipole on the mushroom surface is accurate. This confirms the bandwidth exists where the mushroom surface restores the antenna performance. The performance above a PMC surface does not agree well with the result. This may be due to coupling effects between the antenna and the EBG surface because of their close proximity.

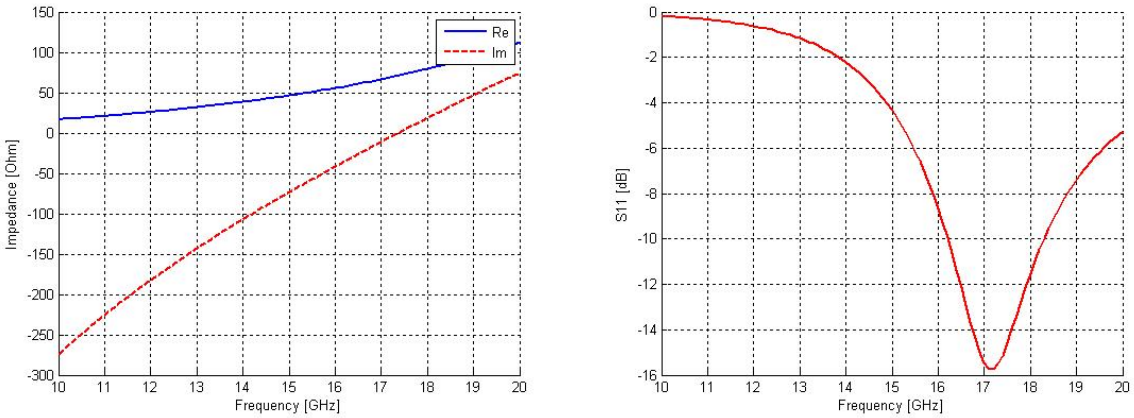

(a) Impedance of the dipole

(b) Return loss of the dipole

Figure 4.1: A Simple 8 mm dipole

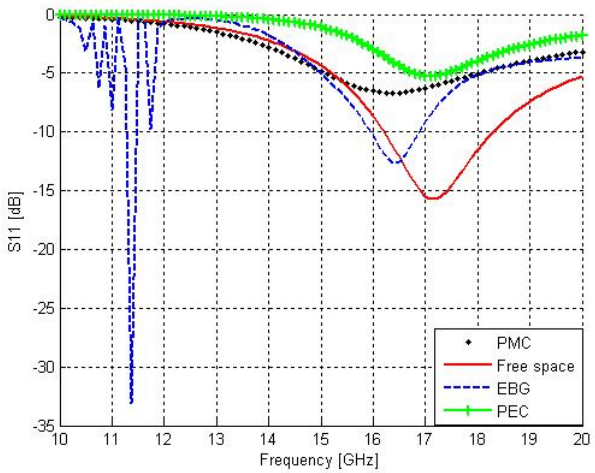

Figure 4.2: An 8 mm Dipole in free space compared with the same dipole on a mushroom EBG, PEC and a PMC surface

The EBG is designed for an 8 *mm* dipole and changing the length may have a different influence compared with the PMC performance. This is however inconclusive and further study is needed.

Although simulations of the mushroom surface give an indication of where the bandgap is, it is not always accurate when placing a low profile antenna above the surface. Placing a low profile antenna above the surface creates complicated interactions between the two and thus the simulated bandgap is at times unpredictable [20].

Figure 4.4 displays the 8 *mm* and the 10 *mm* dipoles on a mushroom surface. The best way to determine the bandgap is to vary the dipole length and find where the performance drops below -10 dB. Such a study is done in [20].

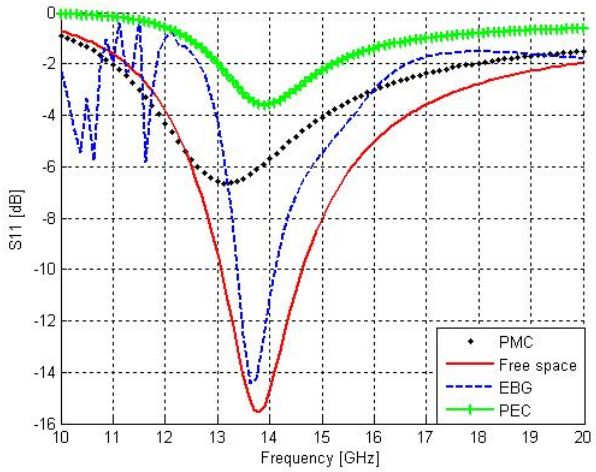

Figure 4.3: An 10 mm Dipole in free space compared with the same dipole on a mushroom EBG, PEC and a PMC surface

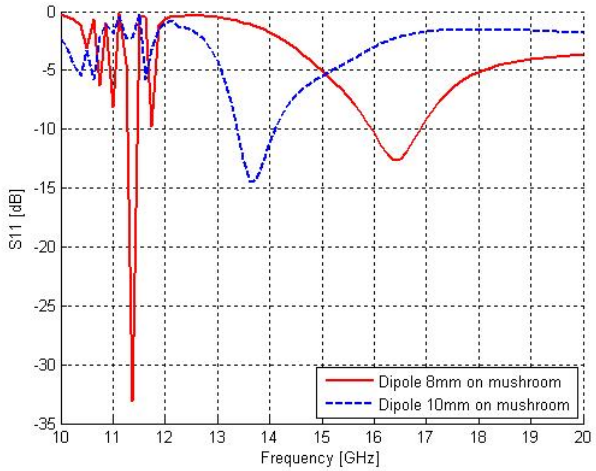

Figure 4.4: Comparison of an 8 mm Dipole and a 10mm Dipole on a mushroom EBG

4.3 Conclusion

The mushroom surface restores the performance of the dipole very well when placed over a ground plane. Placing an antenna above the EBG surface however has an influence on the bandgap and the bandgaps simulated in Chapter 3 are not always that accurate. For an accurate bandgap region the bandgap can be determined by varying the dipole length. Although the design is for a 8 mm dipole, changing the dipole length to 10 mm results in a good return loss indicating that the 10 mm dipole falls in the EBG bandgap.

Further study is needed to determine what influence the coupling effects have on the dipole and the EBG surface because of their close proximity. This may indicate why the PMC surface is consistent with the 8 mm dipole and not with the 10 mm dipole.

Chapter 5

Wide-band Topology: Log-Periodic Dipole Array over a Mushroom EBG

5.1 Introduction

In the previous chapter a dipole over an EBG groundplane had a similar performance to a dipole in free space. Promising results were delivered which suggests that the groundplane acts as a PMC over a certain band. The dipole length can be changed over the same mushroom surface and still yields good results. The problem is still to get the groundplane to perform over a wider band.

The solution proposed and implemented here is to place a low profile LPDA over a mushroom EBG. The LPDA has a broader bandwidth than a single dipole. Fortunately the mushroom EBG is scalable. If the base dipole element of the LPDA works above an EBG surface the rest of the elements' EBG surfaces can be scaled accordingly. In this chapter two LPDA designs are discussed; the wire LPDA and the planar LPDA.

5.2 Wire Log-Periodic Dipole Array

Firstly a small wire LPDA is designed. The LPDA is kept small and simple to keep simulation time down and to receive results quicker. The $10\,mm$ dipole on the mushroom surface of Chapter 4 has good performance. This will form the base from which the wire LPDA and mushroom surface will be designed.

To simplify the design and decrease simulation time a small four element LPDA is designed. Using equations from [21] the following design variables are calculated for the wire LPDA:

- $\tau = 0.93$ (Scaling factor)
- $\sigma = 4.5\,mm$ (Base element spacing)
- $N = 4$ (Number of elements)
- $l_{max} = 10\,mm$ (Base element length)
- $z_a = 365.8\,\Omega$ (Average characteristic impedance)

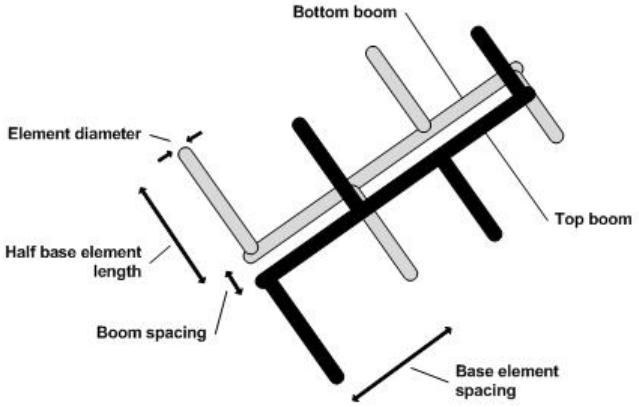

Figure 5.1: A four element wire LPDA

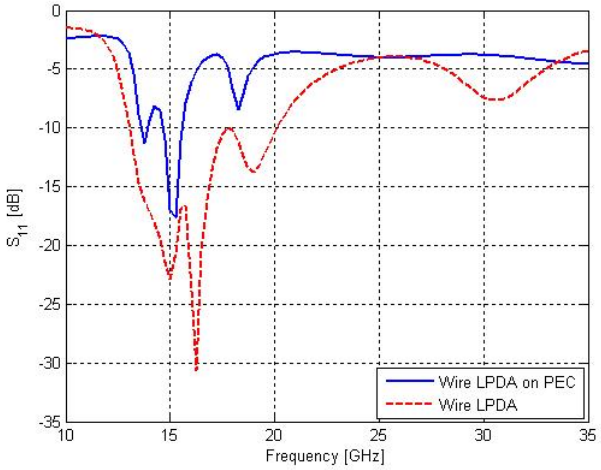

Figure 5.2: Simulated wire LPDA and wire LPDA on PEC

- $s = 0.2\,mm$ (Boom spacing)
- $d = 0.1\,mm$ (Wire diameter)

The model is simulated using FEKO. The return loss of the simulated LPDA is shown in figure 5.2 along with the result of placing the LPDA $1.5\,mm$ above a PEC groundplane. Using -10 dB as the indication of the bandwidth, the band starts at 13.05 GHz and ends at 20.12 GHz. It can also be seen how the PEC surface significantly degrades the LPDA performance.

The next step is to implement the mushroom EBG. One row of mushroom EBG cells is placed beneath each dipole element of the LPDA. The design variables are as follows:

- $a = 3.5\,mm$ (Period of unit cell)
- $g = 0.2\,mm$ (Capacitive gap width)
- $r = 0.05\,mm$ (Via radius)

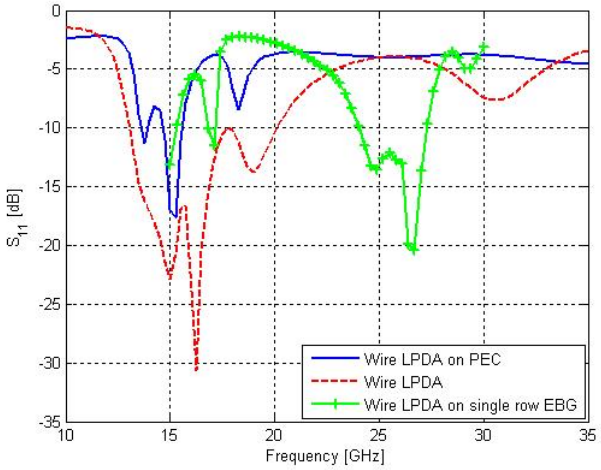

Figure 5.3: Return loss of a LPDA over one row mushroom cells showing that a one row mushroom surface does not perform well

- $H_{lpda} = 0.5\,mm$ (Height of LPDA above mushroom surface)
- $H_{sub} = 1\,mm$ (Height of substrate beneath mushroom surface)
- $\epsilon_r = 2.2$ (Substrate relative permittivity)

The model and the simulated return loss can be seen in figure 5.3. From the result it can be seen that the EBG surface restores the performance of the LPDA from that of a PEC surface. The frequency band is shifted up considerably; this can be because of coupling effects between the antenna and the EBG surface with their close proximity. Further study is needed to confirm this complicated interaction. The band starts at 24 GHz and stops at 27.28 GHz with a percentage of 12.8 % (using -10 dB as reference). The bandgap is smaller than a LPDA in free space with a band of 42.6 %.

To improve the design, two rows of mushroom cells are placed under the LPDA. A challenge with this design is that the spacing between elements should be sufficient to fit the EBG surface underneath it. Increasing the spacing between elements degrades the LPDA performance. The mushroom EBG should be scaled down to accommodate the LPDA. To fit the mushroom the period of the base mushroom cells are changed to $a = 2.2\,mm$. The model can be seen in figure 5.4.

The simulated return loss for the model is shown in figure 5.5, with a reference impedance of 150 Ω. S_{11} is shown with the wire LPDA in free space compared with the wire LPDA over an EBG, a PEC and a PMC surface. As with the single row design the band is shifted up considerably. The band starts at 19.3 GHz and stops at 31.2 GHz with a percentage of 47.1 % (using -10 dB as reference). It is evident that the double row mushroom surface has improved on the performance of the single row mushroom considerably, and shows a similar performance to the PMC surface at a reference impedance of 150 Ω. Unfortunately the band is shifted upwards as with the single row design and further study is needed.

There exists a compromise between scaling the EBG and scaling the LPDA element spacing. Decreasing the EBG dimensions increases the operating frequency, while increasing the base

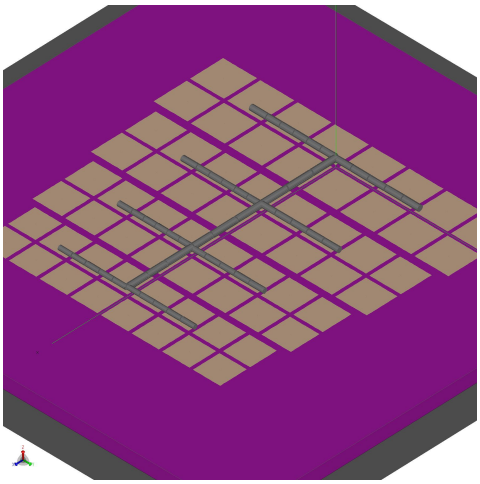

Figure 5.4: Wire LPDA on double row mushroom surface

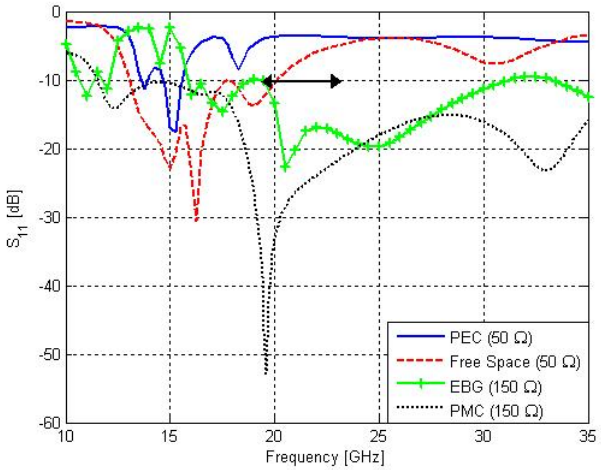

Figure 5.5: Return loss of a wire LPDA on a double row mushroom surface. The arrowed line indicates the EBG's reflection phase bandwidth (figure 5.6).

element length will degrade the antenna performance. In this case the EBG dimensions are decreased to a period of $a = 2.2\,mm$ and the element spacing is kept the same to keep the antenna performance the same. The analytical model of Chapter 2.2 is used to analyse the smaller mushroom structure, equation 2.3.15, and the reflection phase is shown in figure 5.6. The designed antenna frequency of 15 GHz does not fall within the predicted EBG bandwidth between 19.26 GHZ and 23.1 GHz. As stated in Chapter 4 the bandwith of the EBG is not always accurate in close proximity with an antenna. Further study, as mentioned before, may indicate how the EBG band can coincide with the antenna frequency. Keeping the EBG dimensions the same and increasing the antenna element spacing is not investigated and is a study for further work on this topic.

Figure 5.7 shows gain plots at different frequencies. A normal LPDA has a unidirectional radiation pattern to the apex of the structure, looking at figures 5.7(c) and 5.7(d) it can be seen how the ground plane pushes the radiation pattern upwards. This is expected because the

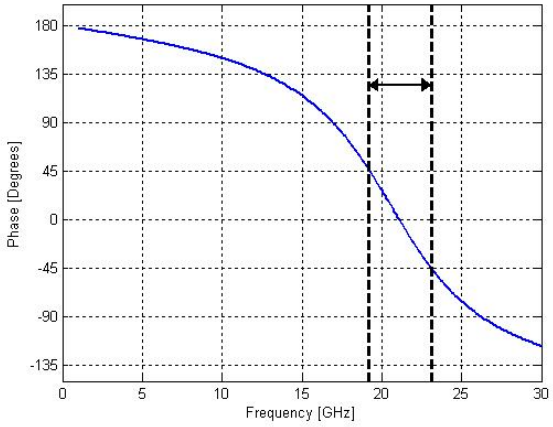

Figure 5.6: Reflection phase of the base element mushroom EBG cells

groundplane is parallel to the LPDA E-field and it prevents radiation along ground.

5.3 Planar Log-Periodic Dipole Array

It is not practical to build a wire LPDA for the high frequency band the model is designed for, thus it is better to convert the model to a planar LPDA. For the planar LPDA the same design dimensions are used as the wire LPDA. Instead of the wire diameter of $0.1\,mm$ the element width is $w = 0.5\,mm$. The mushroom EBG dimensions also stay the same. The model can be seen in figure 5.8.

A simulation is run using FEKO. The return loss of the LPDA is shown in figure 5.9, with a reference impedance of $90\,\Omega$. The return loss of the wire LPDA is also shown in figure 5.9. The bandwidth starts at 15.4 GHz and stops at 30.1 GHz, using -10 dB as reference. The result corresponds well with the wire LPDA and has a lower s_{11} floor, which helps the bandwidth to start at a lower frequency as the wire LPDA. The gain is shown in figure 5.10. It also corresponds very well with the wire LPDA gain results, but at $\theta = 30$ the gain is a bit less for the planar LPDA. The maximum gain for the planar LPDA stays high above 30 GHz, where the wire LPDA maximum gain starts to drop.

To verify the results the same model is designed using CST Microwave Studio, Appendix B, and compared with the FEKO model. The return loss is shown in figure 5.11. Both models are at a reference impedance of $50\,\Omega$. The CST model's band starts at 24.81 GHz and stops at 33.49 GHz, with a percentage of 29.8 %. The FEKO model's band starts at 24.14 GHz and stops at 31.08 GHz, with a percentage of 25.1 %. The CST model performs better, but the simulated results compare well.

5.4 Measurements

For further verification the CST model is compared with measurements done with a manufactured model. Because of manufacturing constraints the model is scaled to three times its size.

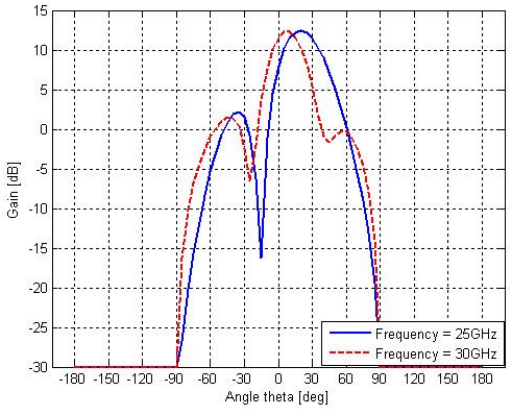

(a) Total gain over theta

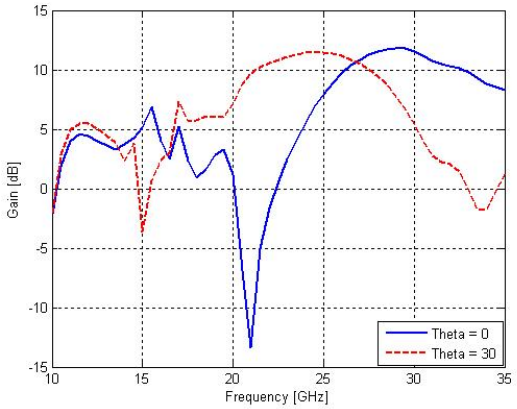

(b) Total gain over frequency

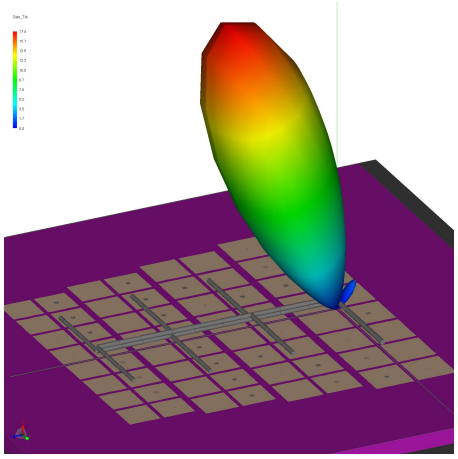

(c) Linear 3D gain at 25 GHz

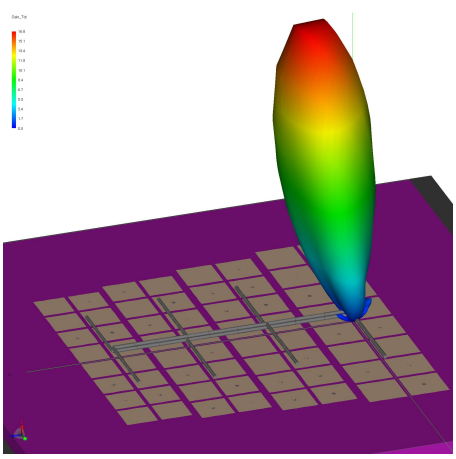

(d) Linear 3D gain at 30 GHz

Figure 5.7: Gain of the wire LPDA on a mushroom EBG

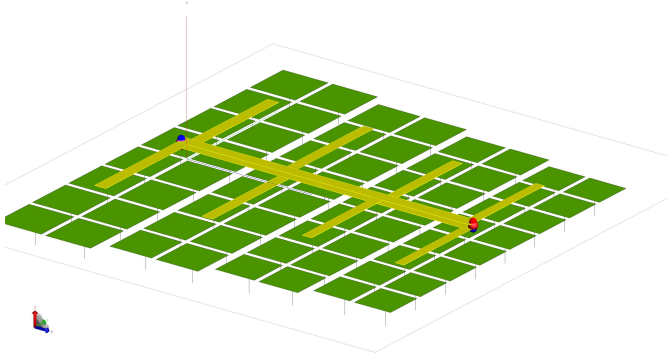

Figure 5.8: A planar LPDA on a mushroom EBG

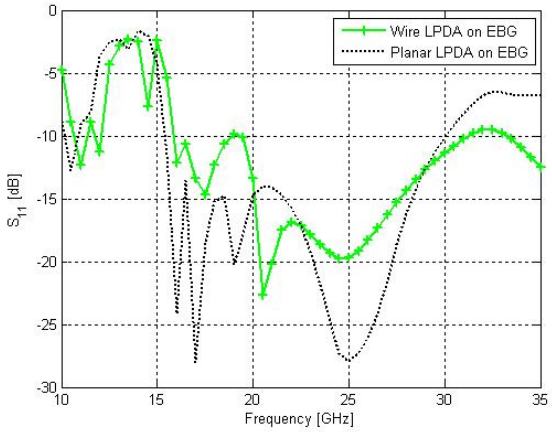

Figure 5.9: Planar LPDA on double row mushroom surface

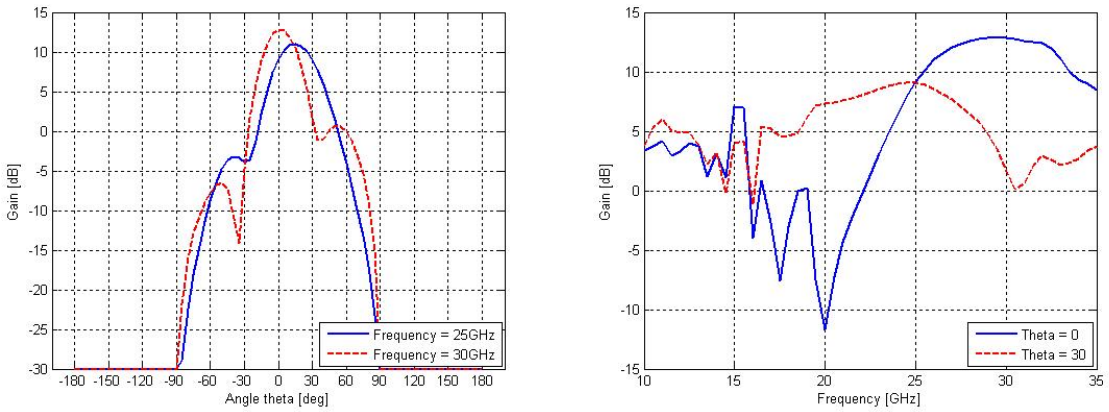

(a) Total gain over theta

(b) Total gain over frequency

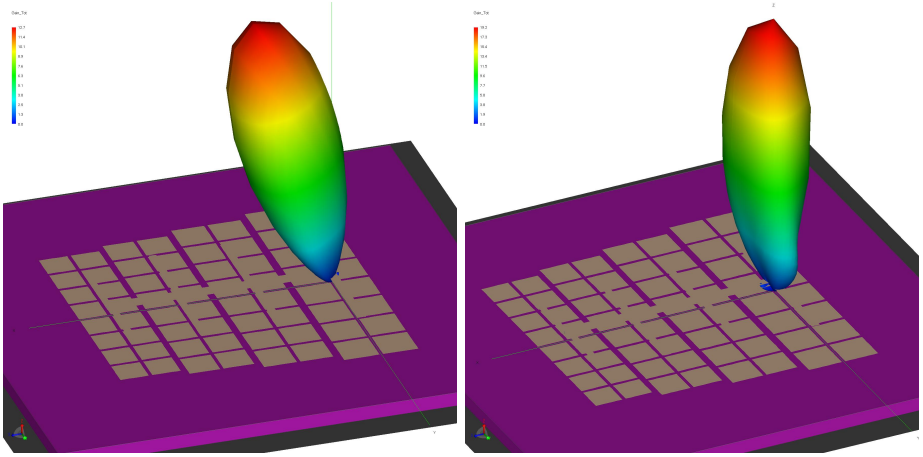

(c) Linear 3D gain at 25 GHz

(d) Linear 3D gain at 30 GHz

Figure 5.10: Gain of the planar LPDA on a mushroom EBG

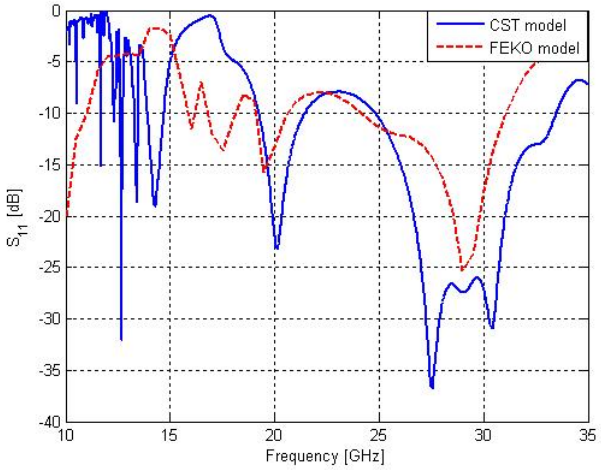

Figure 5.11: Return loss of a CST model vs. a FEKO model

The heights are however not scaled. The available heights from the manufacturer which were used are as follow:

- $H_{lpda} = 1\,mm$ (Height of LPDA above mushroom surface)
- $H_{sub} = 0.7874\,mm$ (Height of substrate beneath mushroom surface)
- $s = 0.127\,mm$ (Boom spacing)

The measurement is done using a HP8510 network analiser. The reference impedance is $50\,\Omega$. The return loss is shown in figure 5.12. The model does not have a good return loss at lower frequencies, as is expected from the height constraints. The measurement and the CST simulation has an accurate match, thus the CST simulation is reliable.

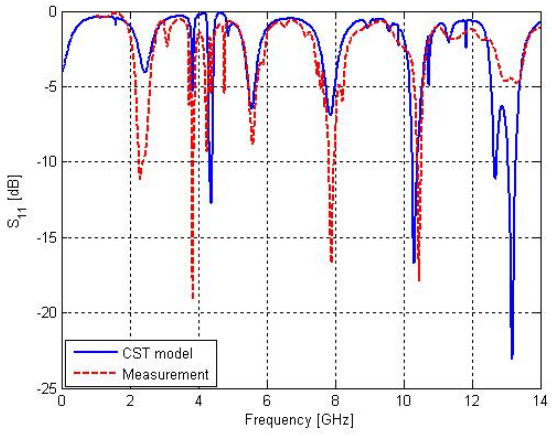

Figure 5.12: Planar LPDA on double row mushroom surface

5.5 Conclusion

This chapter illustrates how a mushroom EBG can be used for a wide-band LPDA. Fortunately the EBG is scalable. This enables the EBG to be scaled along with each dipole element.

Using one row of mushroom cells restores the antenna performance but at a smaller bandwidth; while two rows of mushroom cells not only restore the antenna performance but also improves the bandwidth. The frequency shift may be a result of the coupling effect between the antenna and the EBG surface in close proximity and further study is needed. Looking at the far field results it can also be seen how the groundplane pushes the pattern upwards.

For the double row mushroom surface the EBG dimensions are decreased to fit beneath the LPDA and the antenna element spacing is kept the same. For future study keeping the EBG dimensions the same and increasing the antenna element spacing can be investigated.

A planar LPDA is also designed. For high frequencies it is more practical to convert the wire LPDA to a planar one. With the same design dimensions the planar LPDA performs similar to the wire LPDA.

A model designed using CST Microwave Studio is compared with the FEKO model. The CST model performs better, but the simulated results compare well. The CST model is then compared with the return loss measurements done with a manufactured model. The results are a match and therefore the CST simulation is reliable.

Chapter 6

Conclusion

For the first task the wide-band performance of typical EBG structures are investigated with three EBG surfaces being considered. These surfaces include the JC-EBG, the dumbbell and the mushroom.

For the design process a good analytical model is needed. Chapter 2 investigates some models. A good model for predicting the reflection phase of a mushroom EBG is discussed [13]. This model gives a good platform from which the design can be launched.

Investigating the three typical EBG surfaces gives a good indication of their properties. There are two bandgap regions. The one where surface waves are suppressed and the other where incident waves are reflected with no phase shift.

A parameter sweep is done with all three EBG surfaces. This study helps with the design process. Knowing what influence each variable has on the EBG performance can make the design process less time consuming. From the study it can be seen that the period of each EBG unit cell should be the base of the design, as expected. The results suggest that the mushroom surface has the best properties for implementation with a low-profile wide-band antenna.

When an antenna approaches a groundplane the performance of the antenna is degraded. A narrow-band topology is used to test a low profile dipole antenna placed above a mushroom surface. The results indicate how the EBG restores the antenna performance. Varying the dipole length indicates how the EBG performs over a wide band. The band is however not wide enough to accommodate a LPDA.

Further study is needed to determine what influence the coupling effects have on the dipole and the EBG surface because of their close proximity. This may indicate why the PMC surface is consistent with the $8\,mm$ dipole and not with the $10\,mm$ dipole.

For the wide-band topology a low profile wire LPDA is placed on top of a mushroom surface. The EBG surface is scalable and therefore the surface is scaled down along with each dipole element of the LPDA. Compared with a LPDA over a PEC groundplane a design with one row mushroom cells below each dipole element restores the performance. The bandwidth is however less than that of a LPDA in free space and the frequency of the band is shifted higher. The frequency shift may be a result of the coupling effect between the antenna and the EBG surface in close proximity and further study is needed.

To improve on the one row mushroom design two rows are placed below each dipole element. This shows considerable improvement from the one row mushroom design. Again the frequency

of the band is shifted higher than a LPDA in free space, but it has a wider bandwidth. Radiation along ground is prevented because of the groundplane parallel to the LPDA E-field, this results in the gain pattern being pushed upwards.

For the double row mushroom surface the EBG dimensions are decreased to fit beneath the LPDA and the antenna element spacing is kept the same. For future study keeping the EBG dimensions the same and increasing the antenna element spacing can be investigated.

A model designed using CST Microwave Studio is compared with the FEKO model. The CST model performs better, but the simulated results compare well. The CST model is then compared with the return loss measurements done with a manufactured model. The measurement does not have a good return loss as a result of manufacturing constraints limiting the various heights of the structure. The results between the measurement and the CST simulation are a match and therefore the CST simulation is reliable.

The second proposed task is achieved by scaling EBG cells beneath a low profile LPDA. This mechanism results in a wide-band performance for PMC operation.

Appendices

Appendix A

Formulas and Functions

A.1 The Hankel Function of the Second Kind

The Hankel function is also known as the Bessel function of the third kind. Bessel functions are important for solving wave propagating problems. The Hankel function of the second kind is as follows [15]:

$$H_{\alpha}^{(2)}(x) = \frac{J_{-\alpha}(x) - e^{\alpha\pi i} J_{\alpha}(x)}{-i\, sin(\alpha\pi)} \tag{A.1.1}$$

with J_{α} the Bessel function.

A.2 Derivation of the Boundary Condition for the Reflection Phase Analytical Model

This section's intent is to show the steps of deriving equation (2.3.5). The necessary equations (2.3.2, 2.3.3 and 2.3.4) are listed again below for easier access.

$$E_{x0}^{w} = -\frac{\eta}{4k}\left(k^2 - k_x^2\right) I e^{-jk_x x} H_0^{(2)}\left(\sqrt{k^2 - k_x^2}\, r_0\right) \tag{A.2.1}$$

$$E_x^{loc} = E_x e^{-jk_x x} - \frac{\eta}{2k}\left(k^2 - k_x^2\right) I e^{-jk_x x} \sum_{n=1}^{\infty} cos\left(k_y n d\right) H_0^{(2)}\left(\sqrt{k^2 - k_x^2}\, n d\right) \tag{A.2.2}$$

$$E_x^{loc} + E_{x0}^{w} = Z I^{-jk_x x} \tag{A.2.3}$$

The sum of the Hankel functions in (A.2.2) can be calculated using [14]:

$$\sum_{n=1}^{\infty} cos\left(k_y n d\right) H_0^{(2)}\left(\sqrt{k^2 - k_x^2}\, n d\right) = \frac{1}{|k_z|\, d} - \frac{1}{2} + \frac{j}{\pi}\left[log\frac{\sqrt{k^2 - k_x^2}\, d}{4\pi} + \right.$$
$$\left. \gamma + \frac{1}{2} {\sum_{n=-\infty}^{\infty}}' \left(\frac{2\pi}{\sqrt{\left(2\pi n + k_y d\right)^2 - \left(k^2 - k_x^2\right) d^2}} - \frac{1}{|n|} \right) \right] \tag{A.2.4}$$

Where γ is the Euler constant, $\gamma \approx 0.5772$ [14]. Substituting (A.2.4) into (A.2.2) gives:

$$E_x^{loc} = E_x e^{-jk_x x} - \frac{\eta}{2k}\left(k^2 - k_x^2\right) I e^{-jk_x x}\left\{\frac{1}{|k_z|\,d} - \frac{1}{2} + \frac{j}{\pi}\left[log\frac{\sqrt{k^2-k_x^2}\,d}{4\pi} + \right.\right.$$
$$\left.\left.\gamma + \frac{1}{2}\sum_{n=-\infty}^{\infty}{}'\left(\frac{2\pi}{\sqrt{\left(2\pi n + k_y d\right)^2 - \left(k^2 - k_x^2\right)d^2}} - \frac{1}{|n|}\right)\right]\right\} \tag{A.2.5}$$

For (A.2.1) the Hankel function can be replaced by its asymptotic expression for small arguments, assuming $k_{r_0} \ll 1$:

$$H_0^{(2)}\left(\sqrt{k^2-k_x^2}\,r_0\right) \approx 1 - j\frac{2}{\pi}\left(log\frac{\sqrt{k^2-k_x^2}\,r_0}{2} + \gamma\right) \tag{A.2.6}$$

Substituting (A.2.6) into (A.2.1) gives:

$$E_{x0}^{w} = -\frac{\eta}{4k}\left(k^2 - k_x^2\right) I e^{-jk_x x}\left[1 - j\frac{2}{\pi}\left(log\frac{\sqrt{k^2-k_x^2}\,r_0}{2} + \gamma\right)\right] \tag{A.2.7}$$

Now substituting (A.2.5) and (A.2.7) into (A.2.3), in terms of ZI, gives:

$$\begin{aligned}
ZI &= E_x - \left(\frac{\eta}{2k}\left(k^2 - k_x^2\right) I\right)\left\{\frac{1}{|k_z|\,d} + \frac{j}{\pi}\left[log\frac{\sqrt{k^2-k_x^2}\,d}{4\pi} + \right.\right.\\
&\quad \left.\gamma + \frac{1}{2}\sum_{n=-\infty}^{\infty}{}'\left(\frac{2\pi}{\sqrt{\left(2\pi n + k_y d\right)^2 - \left(k^2 - k_x^2\right)d^2}} - \frac{1}{|n|}\right)\right] -\\
&\quad \left.\frac{j}{\pi}\left(log\frac{\sqrt{k^2-k_x^2}\,r_0}{2} + \gamma\right)\right\}\\
&= E_x - \left(\frac{\eta}{2k}\left(k^2 - k_x^2\right) I\right)\left\{\frac{1}{|k_z|\,d} + \frac{j}{\pi}\left[log\frac{\sqrt{k^2-k_x^2}\,d}{4\pi} - log\frac{\sqrt{k^2-k_x^2}\,r_0}{2} + \right.\right.\\
&\quad \left.\left.\frac{1}{2}\sum_{n=-\infty}^{\infty}{}'\left(\frac{2\pi}{\sqrt{\left(2\pi n + k_y d\right)^2 - \left(k^2 - k_x^2\right)d^2}} - \frac{1}{|n|}\right)\right]\right\}\\
&= E_x - \frac{\eta}{2k}\left(k^2 - k_x^2\right) I\left\{\frac{1}{|k_Z|\,d} + \frac{j}{\pi}\left[log\frac{d}{2\pi r_0} + \right.\right.\\
&\quad \left.\left.\frac{1}{2}\sum_{n=-\infty}^{\infty}{}'\left(\frac{2\pi}{\sqrt{\left(2\pi n + k_y d\right)^2 - \left(k^2 - k_x^2\right)d^2}} - \frac{1}{|n|}\right)\right]\right\}\\
&= \underline{(2.3.5)}
\end{aligned}$$

A.3 Simplification of the Surface Current Density for the Reflection Phase Analytical Model

This section's intent is to show the simplification steps used to reach equation (2.3.6), the surface current density. The necessary equations (2.3.5, $\hat{J}$ and 2.3.7) are listed again below for easier access.

$$ZI = E_x - \frac{\eta}{2k}\left(k^2 - k_x^2\right) I\left\{\frac{1}{|k_Z|\,d} + \frac{j}{\pi}\left[log\frac{d}{2\pi r_0} + \frac{1}{2}\sum_{n=-\infty}^{\infty}{}'\left(\frac{2\pi}{\sqrt{(2\pi n + k_y d)^2 - (k^2 - k_x^2)\,d^2}} - \frac{1}{|n|}\right)\right]\right\} \tag{A.3.1}$$

$$\begin{aligned}\hat{J} &= I/d \\ I &= \hat{J}d\end{aligned} \tag{A.3.2}$$

$$\alpha = \frac{kd}{\pi}\left[log\frac{d}{2\pi r_0} + \frac{1}{2}\sum_{n=-\infty}^{\infty}{}'\left(\frac{2\pi}{\sqrt{(2\pi n + k_y d)^2 - (k^2 - k_x^2)\,d^2}} - \frac{1}{|n|}\right)\right] \tag{A.3.3}$$

To find $\hat{J}$ substitute (A.3.2) and (A.3.3) into (A.3.1):

$$\begin{aligned}\hat{J}Zd &= E_x - \frac{\eta}{2k}\left(k^2 - k_x^2\right)\hat{J}d\left[\frac{1}{|k_Z|\,d} + \frac{j}{\pi}\alpha\frac{\pi}{kd}\right] \\ \hat{J}Z &= \frac{E_x}{d} - \frac{\eta}{2k}\left(k^2 - k_x^2\right)\hat{J}\left[\frac{1}{|k_Z|\,d} + \alpha\frac{j}{kd}\right] \\ \hat{J} &= \frac{\frac{E_x}{d}}{Z + \frac{\eta}{2k}\left(k^2 - k_x^2\right)\left(\frac{1}{|k_Z|d} + \alpha\frac{j}{kd}\right)} \\ &= \frac{2}{\eta}\,\frac{E_x}{\frac{2Zd}{\eta} + \frac{d}{k}\left(k^2 - k_x^2\right)\left(\frac{1}{|k_Z|d} + \alpha\frac{j}{kd}\right)} \\ &= \frac{2}{\eta}\,\frac{\frac{|k_Z|}{k}}{\frac{2Zd}{\eta}\frac{|k_Z|}{k} + \frac{|k_Z|}{k}\frac{d}{k}\left(k^2 - k_x^2\right)\left(\frac{1}{|k_Z|d} + \alpha\frac{j}{kd}\right)}E_x \\ &= \frac{2}{\eta}\,\frac{\frac{|k_Z|}{k}}{\frac{2Zd}{\eta}\frac{|k_Z|}{k} + |k_Z|\,d\left(1 - \frac{k_x^2}{k^2}\right)\left(\frac{1}{|k_Z|d} + \alpha\frac{j}{kd}\right)}E_x \\ &= \frac{2}{\eta}\,\frac{\frac{|k_Z|}{k}}{\left(1 - \frac{k_x^2}{k^2}\right)\left(1 + j\alpha\frac{|k_Z|}{k}\right) + \frac{2}{\eta}\frac{|k_Z|}{k}Zd}E_x \\ &= \underline{(2.3.6)}\end{aligned}$$

A.4 Derivation of the Input Impedance for the Reflection Phase Analytical Model

This section's intent is to show the steps of deriving equation (2.3.15). The necessary equations (2.3.12, 2.3.14 and 2.3.13) are listed again below for easier access.

$$\begin{aligned} Z_{g'}^{TM} &= -j\frac{\eta_{eff}}{2\alpha} \\ Z_{g'}^{TE} &= -j\frac{\eta_{eff}}{2\alpha\left(1-\frac{k_0^2}{k_{eff}^2}\frac{sin^2\theta}{2}\right)} \end{aligned} \tag{A.4.1}$$

$$Z_s^{TE} = j\omega\mu\frac{tan\beta h}{\beta} \tag{A.4.2}$$

$$Z_{inp}^{-1} = Z_{g'}^{-1} + Z_s^{-1} \tag{A.4.3}$$

For normal incidence ($\theta = 0$) and no losses, the following equations apply:

$$\begin{aligned} &\mu = \mu_0 \\ &\beta = \omega\sqrt{\mu\,\epsilon_0\,\epsilon_r} \\ &\epsilon_{eff} = \frac{\epsilon_r + 1}{2} \\ &k_{eff} = \omega\sqrt{\mu\,\epsilon_0\,\epsilon_{eff}} = k_0\sqrt{\epsilon_{eff}} \\ &Z_0 = \eta_0 \end{aligned}$$

Now substituting (A.4.1) and (A.4.3) into (A.4.2) gives:

$$
\begin{aligned}
Z_{inp}^{-1} &= \frac{j2\alpha\left(1-\frac{k_0^2}{k_{eff}^2}\,\frac{sin^2\theta}{2}\right)}{\eta_{eff}} + \frac{1}{j\omega\mu}\,\frac{\beta}{tan(\beta h)} \\
&= j\left[\frac{2\alpha\left(1-\frac{k_0^2}{k_{eff}^2}\,\frac{sin^2\theta}{2}\right)}{\eta_{eff}} - \frac{1}{\omega\mu}\,\frac{\beta}{tan(\beta h)}\right] \\
&= j\left[\frac{2\alpha\left(1-\frac{k_0^2}{k_{eff}^2}\,\frac{sin^2\theta}{2}\right)\omega\,\mu\,tan(\beta h)-\beta\,\eta_{eff}}{\eta_{eff}\,\omega\,\mu\,tan(\beta h)}\right] \\
Z_{inp} &= -j\left[\frac{\omega\,\mu\,tan(\beta h)}{2\alpha\left(1-\frac{k_0^2}{k_{eff}^2}\,\frac{sin^2\theta}{2}\right)\omega\,\mu\,tan(\beta h)\,\frac{1}{\eta_{eff}}-\beta}\right] \\
&= \frac{j\,\omega\,\mu\,\frac{tan(\beta h)}{\beta}}{1-2\alpha\left(1-\frac{k_0^2}{k_{eff}^2}\,\frac{sin^2\theta}{2}\right)\omega\,\mu\,\frac{tan(\beta h)}{\beta}\,\frac{1}{\eta_{eff}}} \\
&= \frac{j\,\omega\,\mu\,\frac{tan(\beta h)}{\beta}}{1-2\alpha\left(1-\frac{sin^2\theta}{2\epsilon_{eff}}\right)\omega\,\mu\,\frac{tan(\beta h)}{\beta}\,\sqrt{\frac{\epsilon_0\,\epsilon_{eff}}{\mu_0}}} \\
&= \frac{j\,\omega\,\mu\,\frac{tan(\beta h)}{\beta}}{1-2\alpha\left(1-\frac{sin^2\theta}{2\epsilon_{eff}}\right)\,\frac{tan(\beta h)}{\beta}\,k_{eff}} \\
&= \frac{j\,\omega\,\mu\,\frac{tan(\beta h)}{\beta}}{1-2\,k_{eff}\,\alpha\,\frac{tan(\beta h)}{\beta}\left(1-\frac{1}{\epsilon_r+1}\,sin^2\theta\right)} \\
&= \underline{(2.3.15)}
\end{aligned}
$$

Appendix B

Simulation Setup

The packages used for all the simulations are FEKO and CST Microwave Studio. Here follows a brief description of each package:

FEKO is a computational electromagnetics tool. It uses formulations based on Method of Moments (MoM) and the Finite Element Method (FEM) to analyse EM problems. FEKO consists of various environments. The first environment used is CADFEKO with which a 3D model is built. PREFEKO generates input for the solver. RUNFEKO runs the solver and generates the output. When the solver is complete POSTFEKO is used to view the results of the output.

CST Microwave Studio is based on the Finite Integral Technique (FIT). It is used to solve general electromagnetic problems. A mesh is created and splits the problem into small cells, creating a mesh grid. For each mesh cell the integral form of Maxwell's equations are formulated to solve the problem. Two solvers are used, the transient solver and the eigenmode solver. The transient solver is a time domain solver that calculates the transmission of energy at discrete points in time. The Eigenmode solver calculates the eigenmodes and resonant frequencies.

This chapter will discuss the various simulation setups used in this paper.

B.1 S-parameter Simulation Setup in CST

For this simulation a CAD model is built of the relevant structure in CST Microwave Studio. The model consists of an array of 8x8 EBG cells.

Two discrete ports are manually designed. Each port has a teflon coating and is placed $0.75 \times a$ (a is the length of a single cell) into the bottom left corner and upper right corner. The manually created discrete ports are excited with a plane wave (Figure B.1).

Remember to set the desired frequency, in this case it was 10 GHz to 30 GHz. All the boundary conditions are set to "open (add space)".

Now open the transient solver. Set the desired accuracy, in this case it was -40 dB. Tick the normalise s-parameter box and run the simulation (Figure B.2).

Remember to setup a good mesh. It may also be necessary to increase the steady state criterion passes.

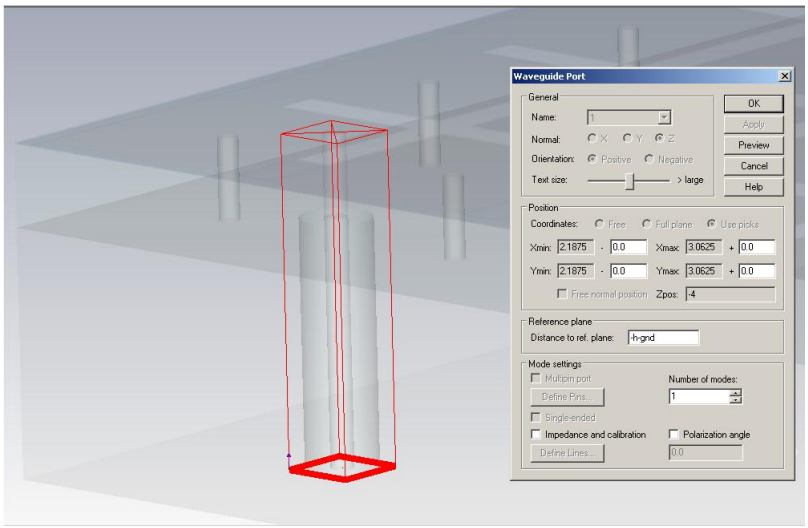

Figure B.1: Setup of the discrete port

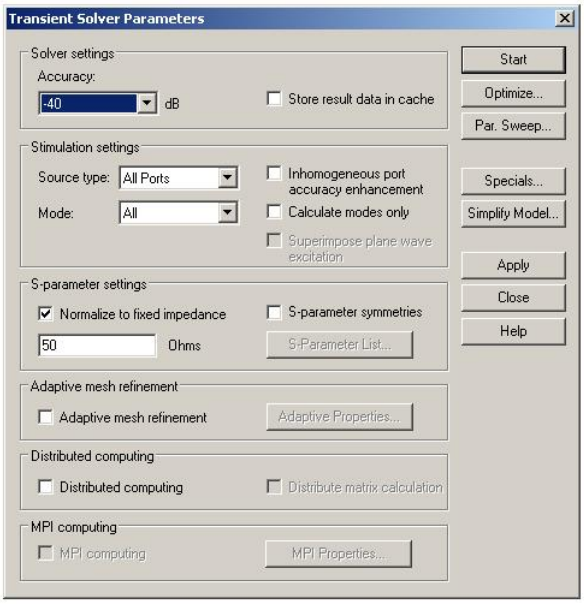

Figure B.2: Setup of the transient solver

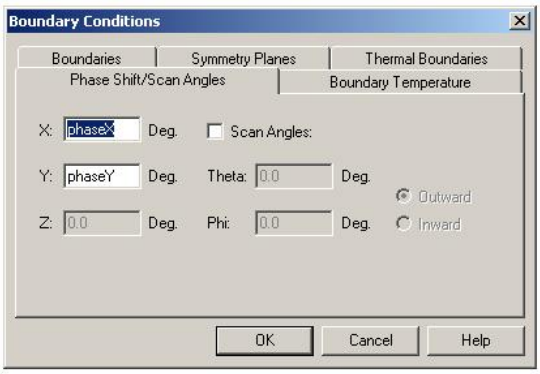

Figure B.3: The "phase shift/scan angles" tab

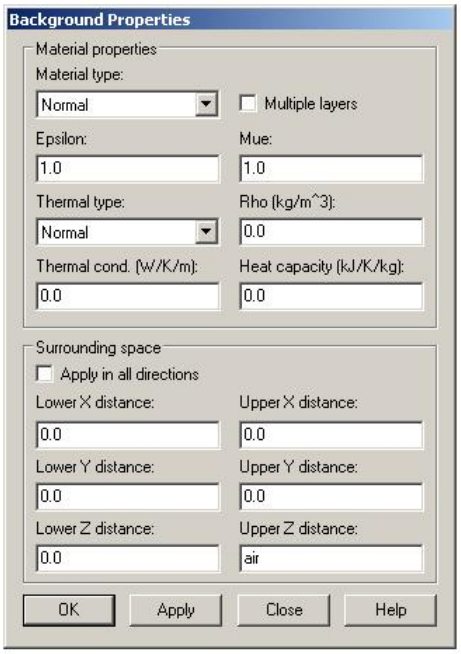

Figure B.4: The background material tab

B.2 Dispersion Diagram Setup in CST

For this simulation a CAD model is built of the relevant structure in CST Microwave Studio. The model consists of a unit cell of the EBG. For an application note see [16].

No ports need to be defined.

Set the boundary conditions for the x- and y-axis to periodic and the z_{min} to electric. For a TE dispersion diagram set the z_{max} to magnetic and for a TM dispersion diagram set it to electric. In the "phase shift/scan angles" tab (Figure B.3) insert variables for the X and Y phases.

Using the Background Material tab (Figure B.4) the upper z distance can be increased by a small amount, this is just to separate the surface from the boundary a bit.

Open the eigenmode solver. Choose the number of modes required and click on parameter

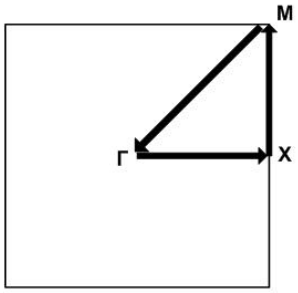

Figure B.5: Brillouin zone of the unit cell

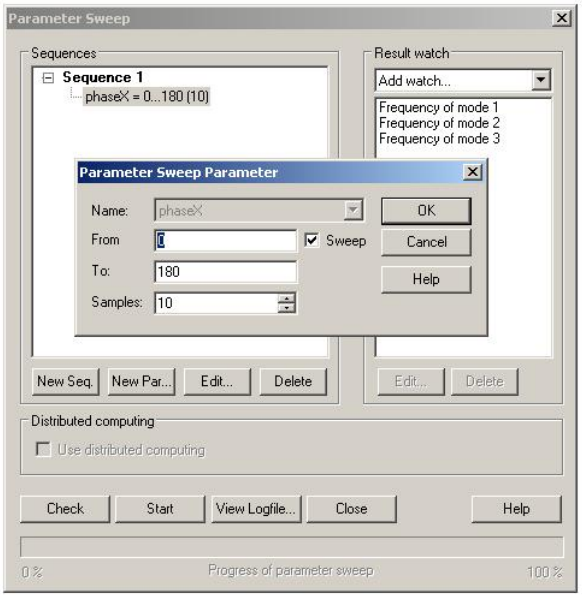

Figure B.6: The parameter sweep tab

sweep. Create a new sequence and a new parameter (Figure B.6). There are three stages to the simulation (see figure B.5):

Γ to X : Set phase-y to zero and sweep phase-x from 0 to 180 degrees.

X to M : Set phase-x to 180 degrees and sweep phase-y from 0 to 180 degrees.

M to Γ : sweep phase-x and phase-y from 0 to 180 degrees.

Γ represents the middle of the Brillouin zone, X the centre of the boundary edge of the Brillouin zone and M the corner of the Brillouin zone.

All that is left is to combine the results of the three stages.

B.3 Reflection Phase Setup in CST

For this simulation a CAD model is built of the relevant structure in CST Microwave Studio. The model consists of an array of 8x8 EBG cells.

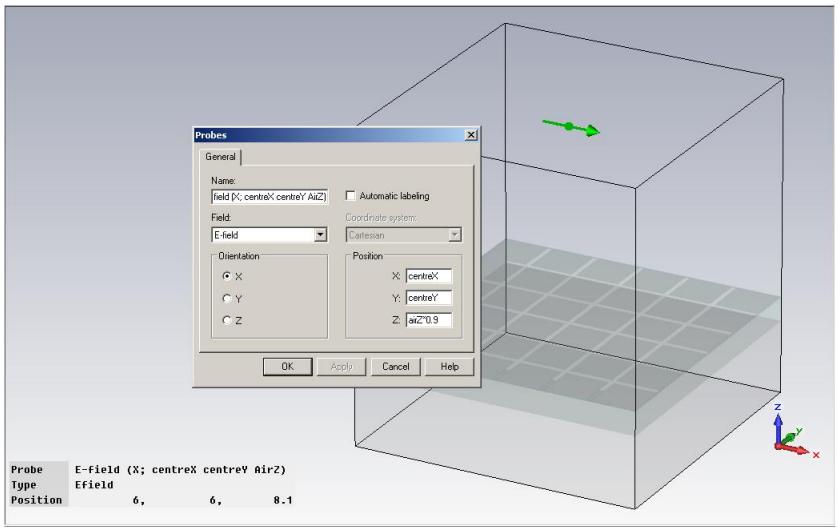

Figure B.7: E-field probe

For the simulation of the reflection phase of a plane wave on the surface requires additional post processing steps. The technique used is called time gating [19].

Set the boundary conditions for the x- and y-axis to periodic, the z_{min} to electric and the z_{max} to open (add space). Open the Background Material tab and insert a value for the upper Z distance. This distance should be high enough to give the plane wave enough time to propagate.

Create an E-field probe. This probe should be located on the centre of the structure, but close to the plane wave (figure B.7).

Set the frequency. The minimum frequency should start at 0 GHz. Now run the transient solver. Remember to create a good mesh.

Using the E-field result of the probe the time gating process can begin. Open the "Template Based Post Processing" tab and follow these steps:

Load E-field : Use the "Load 1D Data File" option to load the E-field time signal generated by the probe.

Separate reflected wave : The first part of the E-field time signal represents the incident wave (Figure B.8) and the latter the reflected wave. The reflected needs to be isolated. Open the "1D Result from 1D Result" option. Choose the "x - sub range" action. Enter the time where the incident and reflected wave splits at "xlow" and the time when the signal ends at "xhigh". Now choose the E-field from the 1D results dropdown bar.

DFT : Open the "1D Result from 1D Result" option and choose the "DFT - phase" action. Choose the reflected wave from the "1D Results" dropdown.

Unwrap : Open the "UnWrap/Wrap of 1D phase data" option and unwrap the new DFT reflection phase.

Load reflected ground wave : The same process as above should be followed for a PEC surface, with the same dimensions as the desired model. Save the ascii file of the reflected ground phase. Choose the "Load 1D Data File" option and load the file.

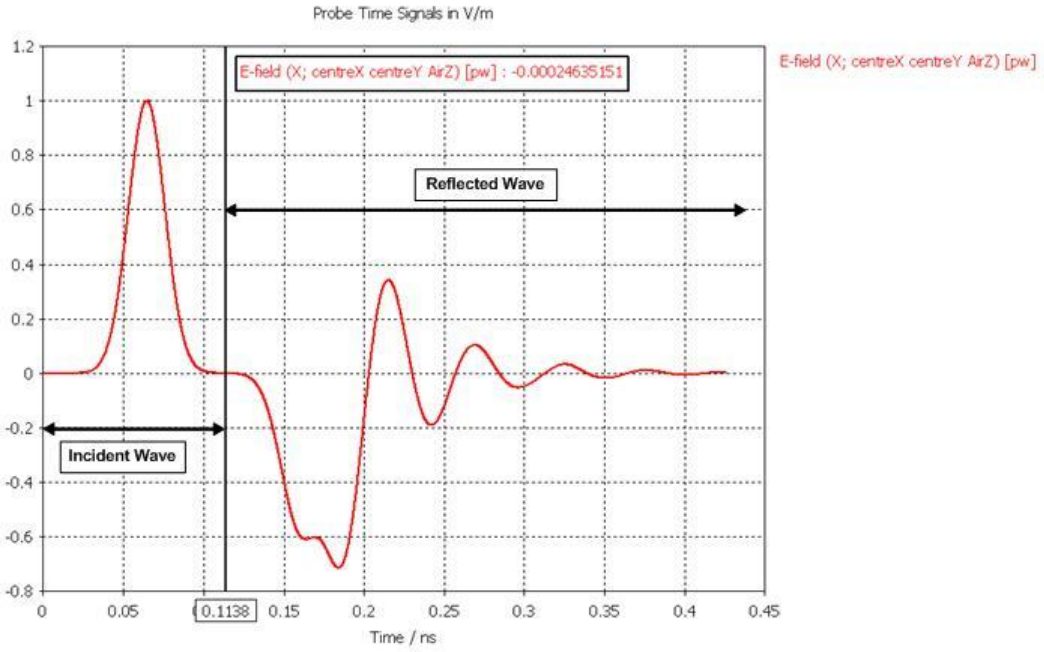

Figure B.8: Separation between the reflected wave and the incident wave of the E-field time signal

Mix results : Open the "Mix 1D Results" option. Subtract the ground phase from the reflected phase and add 180^o.

B.4 Simulations Using FEKO

Open CADFEKO and build the desired 3D model. Create a good mesh; use the local mesh option to create a finer mesh if needed.

For the Dipole as well as the LPDA on a mushroom EBG surface a wire port is used to excite the antenna.

Use the "Define infinite plane" button to define a substrate and a ground plane. See figure B.9.

Set the minimum and maximum frequency and run PREFEKO. Now run RUNFEKO. The output can now be seen using POSTFEKO.

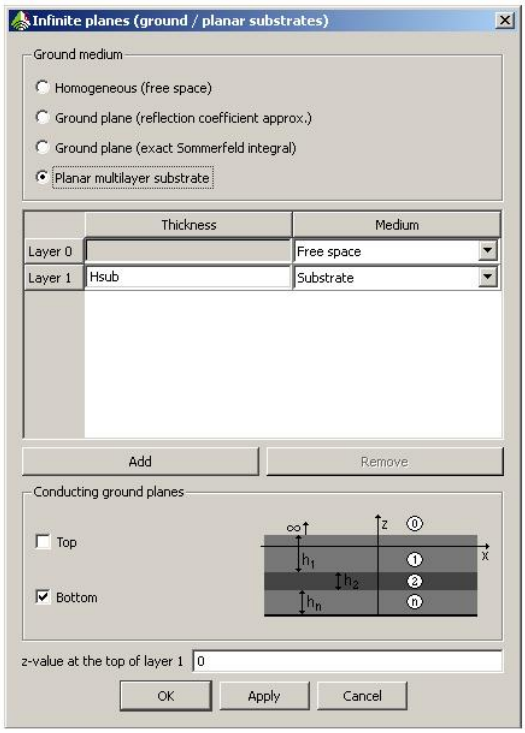

Figure B.9: Infinite ground planes

Appendix C

EBG Parametric Study Results

Figures C.1 to C.6 display the results of the parametric study of three EBG topologies. Figures C.1, C.3 and C.5 display the change in bandwidth when varying the variables. Figures C.2, C.4 and C.6 display three points for each variable, the upper point represents the maximum frequency of the bandgap, the middle point the centre frequency and the lower point the minimum frequency of the bandgap.

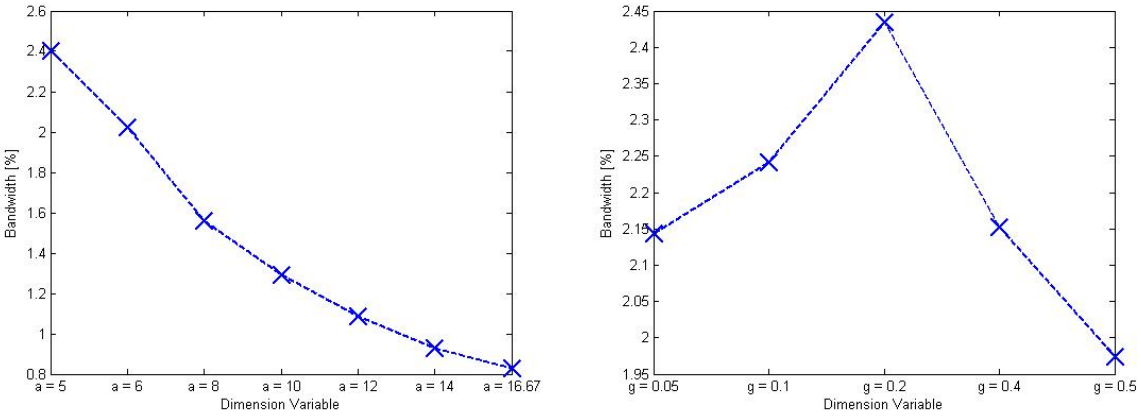

(a) Varying the period

(b) Varying the gap

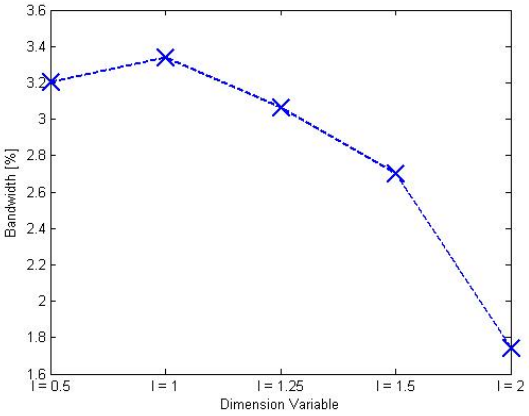

(c) Varying the half-inductor length

Figure C.1: Change in BW when varying the JC-EBG variables

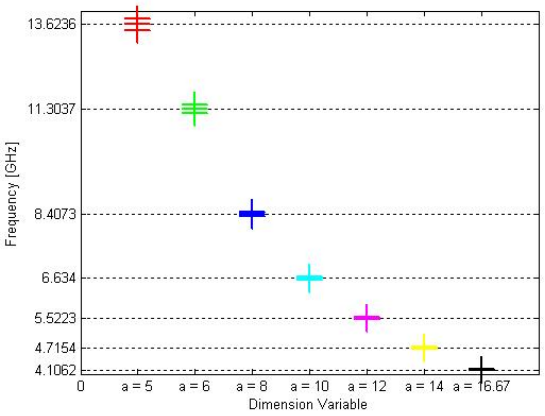

(a) Varying the period

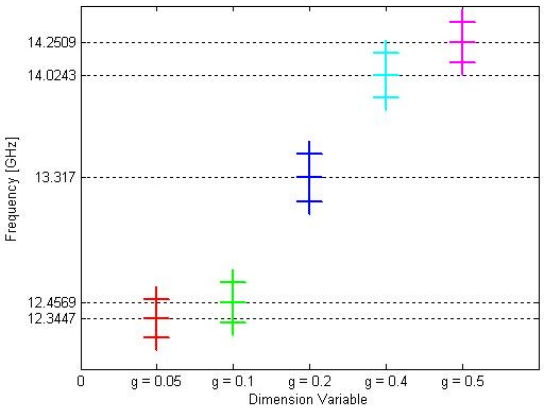

(b) Varying the gap

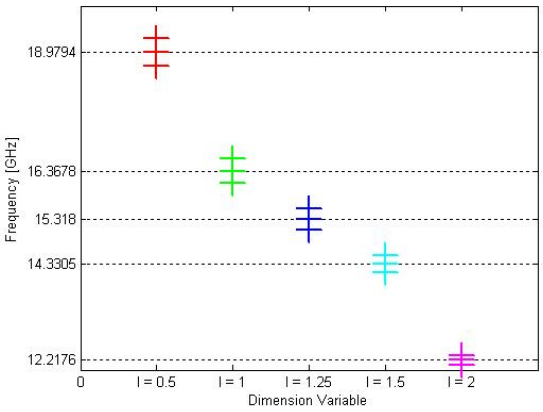

(c) Varying the half-inductor length

Figure C.2: Change in centre frequency when varying the JC-EBG variables

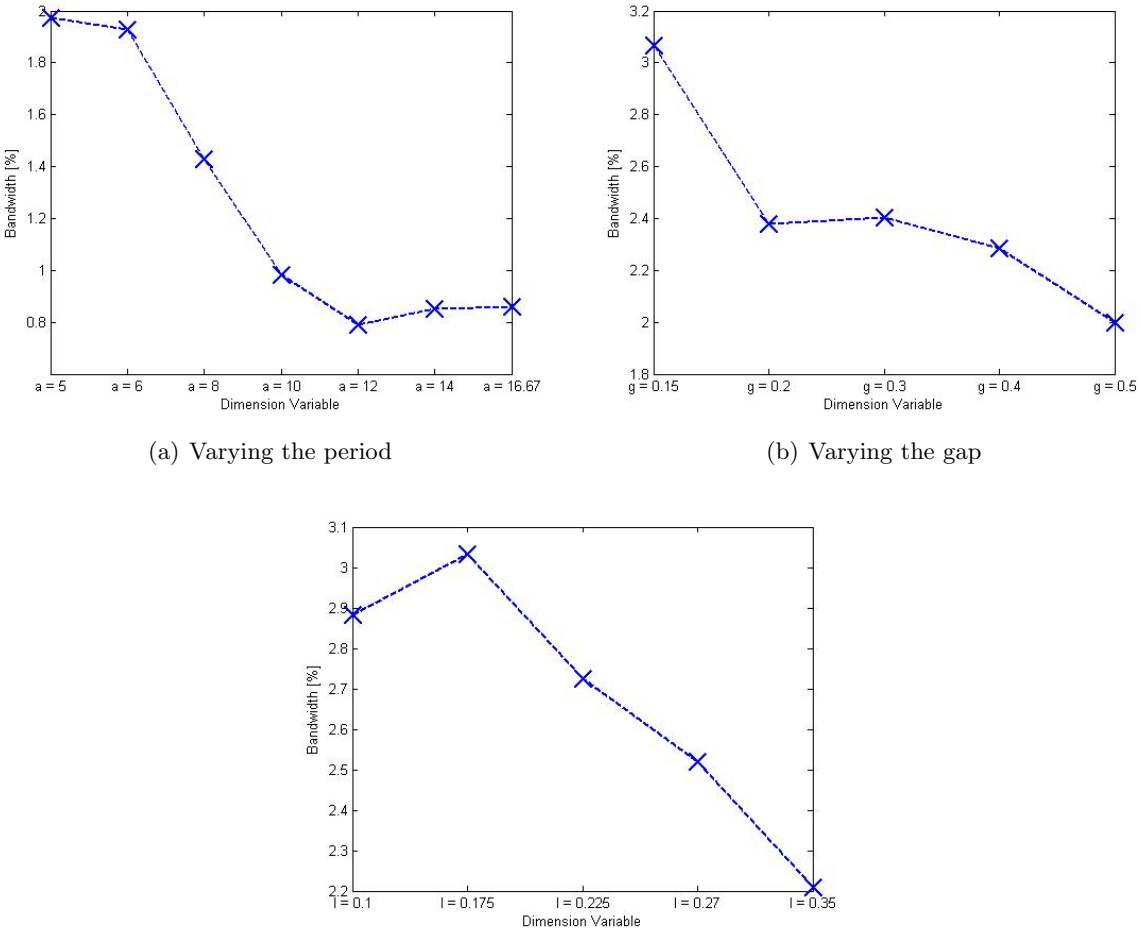

(a) Varying the period

(b) Varying the gap

(c) Varying the half-inductor length

Figure C.3: Change in BW when varying the dumbbell EBG variables

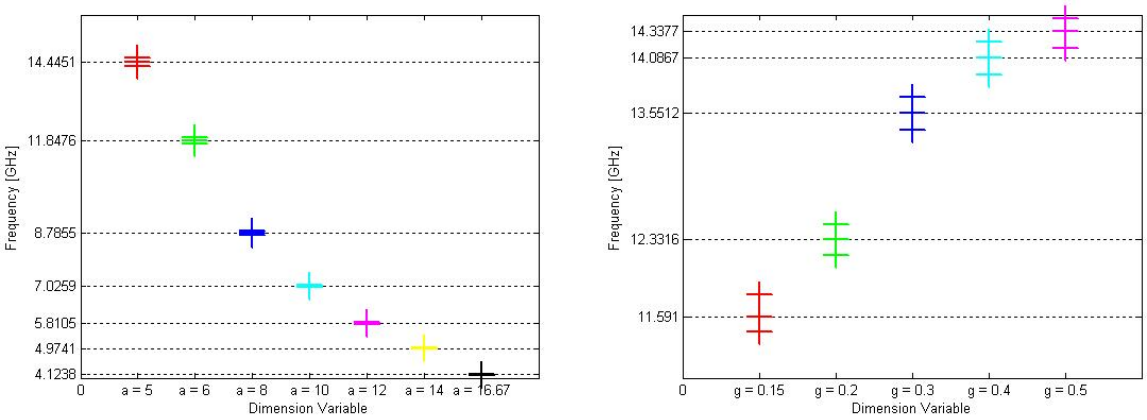

(a) Varying the period

(b) Varying the gap

(c) Varying the half-inductor length

Figure C.4: Change in centre frequency when varying the dumbbell EBG variables

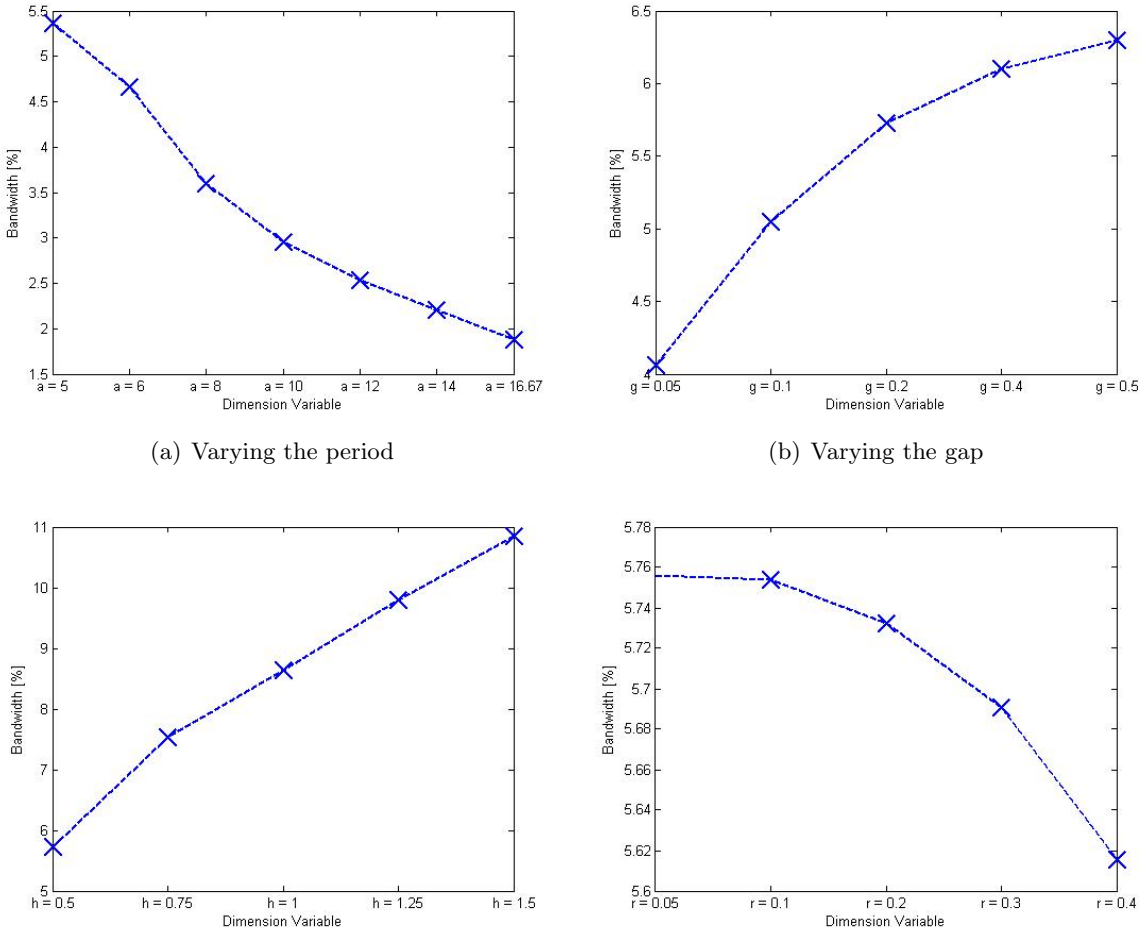

(a) Varying the period

(b) Varying the gap

(c) Varying the height

(d) Varying the via radius

Figure C.5: Change in BW when varying the mushroom EBG variables

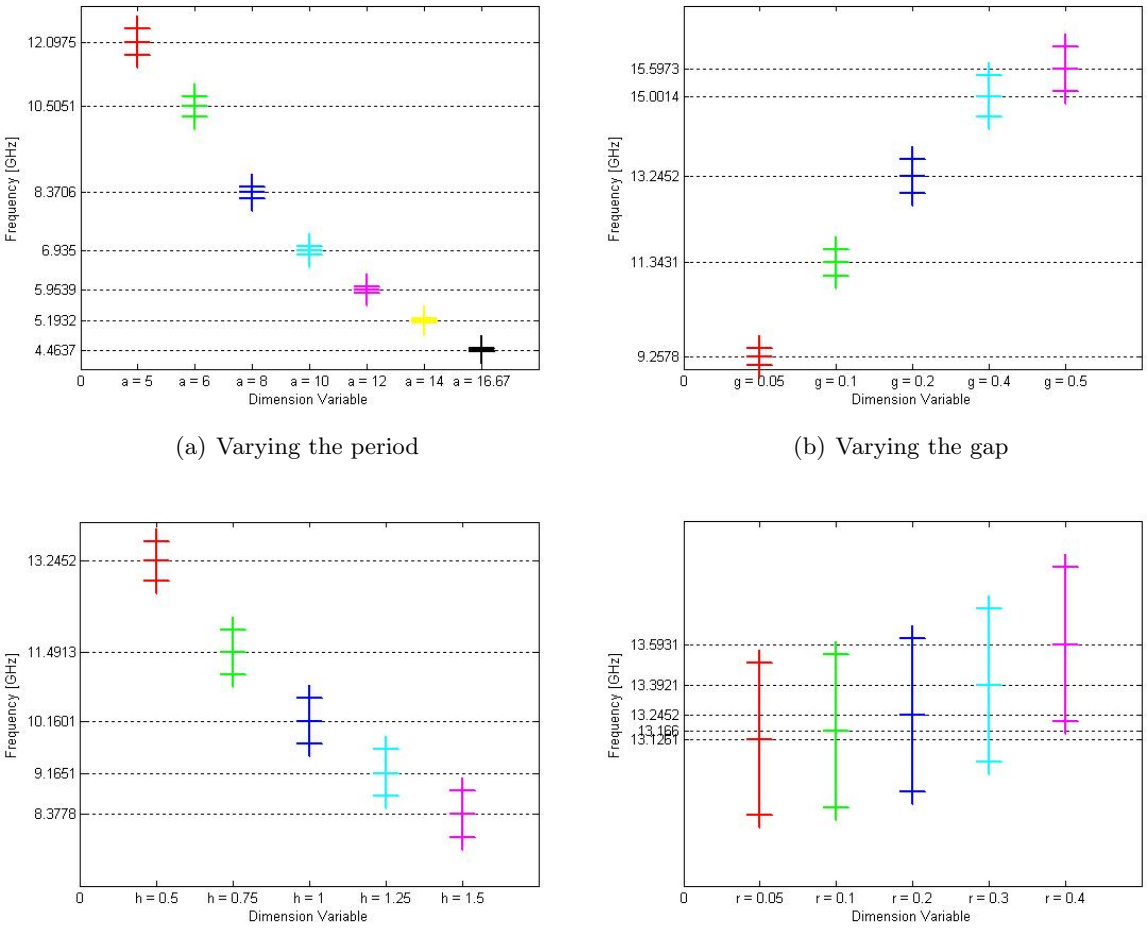

(a) Varying the period

(b) Varying the gap

(c) Varying the height

(d) Varying the via radius

Figure C.6: Change in centre frequency when varying the mushroom EBG variables

Bibliography

[1] D.S. Sievenpiper, *High-Impedance Electromagnetic Surfaces*. Department of Electrical Engineering, Doctor of Philosophy in Electrical Engineering, University of California, 1999.

[2] G. Goussetis, A.P. Feresidis, J.C. Vardaxoglou, *Tailoring the AMC and EBG Characteristics of Periodic Metallic Arrays Printed on Grounded Dielectric Substrate*. IEEE Transactions on Antennas and Propagation, vol. 54, no. 1, January 2006.

[3] A.P. Feresidis, G. Goussetis, S. Wang, J.C. Vardaxoglou, *Artificial Magnetic Conductor Surfaces and Their Application to Low-Profile High-Gain Planar Antennas*. IEEE Transactions on Antennas and Propagation, vol. 53, no. 1, January 2005.

[4] F. Yang, K. Ma, Y. Qian, T. Itoh, *A Uni-planar Compact Photonic-Bandgap (UC-PBG) Structure and Its Applications for Microwave Circuits*. IEEE Transactions on Microwave Theory and Techniques, vol. 47, no. 8, August 1999.

[5] E. Laubscher, R.H. Geschke, *A Novel Uniplanar Electromagnetic Bandgap Unit Cell Design With Reduced Spurious Radiation*. South African Institute of Electrical Engineers, vol. 99, no. 3, September 2008.

[6] Y. Zhang, J. von Hagen, M. Younis, C. Fischer, W. Wiesbeck, *Planar Artificial Magnetic Conductors and Patch Antennas*. IEEE Transactions on Antennas and Propagation, vol. 51, no. 10, October 2003.

[7] E. Laubscher, *Improving Signal Integrity on Printed Circuit Boards by Managing Parasitic Modes*. Department of Electrical & Electronic Engineering, Master of Science in Engineering, University of Stellenbosch, 2007.

[8] S.A. Tretyakov, C.R. Simovski, *Dynamic Model of Artificial Reactive Impedance Surfaces*. Journal of Electromagnetic Waves and Applications, vol. 17, no. 1, pp 131-145, 2003.

[9] M. Rahman, M.A. Stuchly, *Transmission Line-Periodic Circuit Representation of Planar Microwave Photonic Bandgap Structures*. Microwave and Optical Technology Letters, vol. 30, no. 1, July 5 2001.

[10] S. Shahparnia, O.M. Ramahi, *A Simple and Effective Model for Electromagnetic Bandgap Structures Embedded in Printed Circuit Boards*. IEEE Microwave and Wireless Components Letters, vol.15, no. 10, October 2005.

[11] D.M. Pozar, *Microwave Engineering*. John Wiley & Sons Inc, 3rd Edition, 2005.

[12] M. Hosseini, M Hakkak, *Characteristics Estimation for Jerusalem Cross-Based Artificial Magnetic Conductors*. IEEE Antennas and Wireless Propagating Letters, vol. 7, 2008.

[13] O. Luukkonen, C. Simovski, G. Granet, G. Goussetis, D. Lioubtchenko, A.V. Räisänen, S.A. Tretyakov, *Simple and Accurate Analytical Model of Planar Grids and High-Impedance Surfaces Comprising Metal Strips or Patches*. IEEE Transactions on Antennas and Propagation, vol. 56, no. 6, JUNE 2008.

[14] S. Tretyakov, *Analytical Modelling in Applied Electromagnetics*. Artech House Inc, 2003.

[15] M. Abramowitz, I.A. Stegun, eds., *Handbook of Mathematical Functions with Formulas, Graphs, and Mathematical Tables*. Dover publications, inc., New York, 1970.

[16] CST, *How to generate Dispersion Diagrams for Photonic Bandgap Structures*. Application Note for CST Microwave Studio®, MMA, v1.0, April 2006.

[17] F. Yang, K. Ma, Y. Qian, T. Itoh, *A Uniplanar Compact Photonic-Bandgap (UC-PBG) Structure and Its Applications for Microwave Circuits*. IEEE Transactions on Microwave Theory and Techniques, vol. 47, no. 8, August 1999.

[18] F.Yang, K. Ma, Y. Qian, T. Itoh, *A Novel TEM Waveguide Using Uniplanar Compact Photonic-Bandgap (UC-PBG) Structure*. IEEE Transactions on Microwave Theory and Techniques, vol. 47, no. 11, November 1999.

[19] CST, *Calculating reflection coefficients from plane wave excitations using E-Field probes with time gating*. Application Note for CST Microwave Studio®, FDE, ver. 1.0, February 2008.

[20] F. Yang, Y Rahmat-Samii, *Reflection Phase Characterizations of the EBG Ground Plane for Low Profile Wire Antenna Applications*. IEEE Transactions on Antennas and Propagation, vol. 51, no. 10, October 2003.

[21] C.A. Balanis, *Antenna Theory, Analysis and Design*. John Wiley & Sons Inc, 3rd Edition, 2005.

[22] M.Z. Azad, M. Ali, *Novel Wideband Directional Dipole Antenna on a Mushroom Like EBG Structure*. IEEE Transactions on antennas and propagation, vol. 56, no. 5, May 2008.

[23] F. Yang, A. Aminian, Y. Rahmat-Samii, *A Novel Surface-wave Antenna Design Using a Thin Periodically Loaded Ground Plane*. Microwave and Optical Technology Letters, vol. 47, no. 3, November 2005.